Imaging near-surface sharp lateral variations with surface-wave methods — Part 1: Detection and location

Imaging near-surface sharp lateral variations with surface-wave methods — Part 1: Detection and location

Chiara Colombero[1], Cesare Comina[2], and Laura Valentina Socco[1]

[1]Politecnico di Torino, Department of Environment, Land and Infrastructure Engineering (DIATI), c.so Duca degli Abruzzi, 24, Torino 10129, Italy.

E-mail: chiara.colombero@polito.it (corresponding author); valentina.socco@polito.it

[2]Università degli Studi di Torino, Department of Earth Sciences (DST), via Valperga Caluso, 35, Torino 10125, Italy.

E-mail: cesare.comina@unito.it

Chiara Colombero, Cesare Comina, and Laura Valentina Socco, (2019), "Imaging near-surface sharp lateral variations with surface-wave methods — Part 1: Detection and location," *GEOPHYSICS* 84: EN93-EN111.https://doi.org/10.1190/geo2019-0149.1

ABSTRACT

Near-surface sharp lateral variations can be either a target of investigation or an issue for the reconstruction of reliable subsoil models in surface wave (SW) prospecting. Effective and computationally fast methods are consequently required for detection and location of these shallow heterogeneities. Four SW-based techniques, chosen between available literature methods, are here tested for detection and location purposes. All the tested techniques are updated for multifold data and then systematically tested on new synthetic and field data. The selected methods are based on the computation of energy, energy decay exponent, attenuation coefficient and autospectrum. The multifold upgrade is based on stacking of the computed parameters for single-shot or single-offset records and improves readability and interpretation of the final results. Detection and location capabilities are firstly extensively evaluated on a variety of on-purpose built 2D synthetic models, simulating different geometries of the target, embedment conditions and impedance contrasts with respect to the background. The methods are then validated on two field cases: a shallow low-velocity body in a sedimentary sequence and a hard rock site with two embedded subvertical open fractures. For a quantitative comparison, the horizontal gradient of the four parameters is analyzed to establish uniform criteria for location estimation. All the methods show ability in both detecting and locating lateral variations having lower acoustic impedance than the surrounding material, with errors generally comparable or lower than the geophone spacing. More difficulties are encountered in locating targets with higher acoustic impedance than the background. In this configuration, weak contrasts in acoustic impedance, high embedment depths and small dimensions of the discontinuity can prevent from a precise location of the targets.

INTRODUCTION

Near-surface seismic surveys may involve subsurface lateral heterogeneities with strong lateral contrasts in physical and mechanical properties. Typical heterogeneities are objects having lower acoustic impedance than the background. These include cavities, fractures and faults, buried slopes and embedded low-velocity bodies. In other investigations, lateral variations having higher acoustic impedance than the enclosing medium may also be of interest, as in the case of steeply dipping mineralized veins and seams or buried ore bodies.

The presence of these heterogeneities can affect the results of a wide variety of studies, ranging from regional and local geology (Carpentier et al., 2012; Hyslop and Stewart, 2015; Ikeda and Tsuji, 2016) to geotechnical engineering investigations (Hévin et al., 1998; Gischig et al., 2015) or potential hydrogeological and mineral explorations (Bièvre et al., 2012). P- and S-wave tomography may result inadequate to effectively delineate location and depth of these sharp variations with desirable detail due to limitations in ray coverage and behavior of refracted rays, particularly when dealing with low velocity heterogeneities (Colombero et al., 2016; Ikeda and Tsuji, 2016). By contrast, surface waves (SWs) that propagate parallel to the ground surface and with lower attenuation with respect to body waves, may be potentially valuable for detection and imaging of local heterogeneities.

The recognition of sharp lateral changes is also of primary importance for SW data processing itself. Common techniques are indeed aimed at the reconstruction of local 1D subsurface models, neglecting the presence of lateral variations. However, this assumption leads to erroneous velocity models when lateral variations occur at the site. Different strategies have been proposed in literature to overcome this limitation. In case of smooth lateral variations, spatial windowing of the seismic records for dispersion curve estimation was found to offer a good compromise to

reconstruct local properties and gradual changes (Bohlen et al., 2004; Boiero and Socco, 2011). Nevertheless, a different approach is needed in presence of sharp lateral contrasts. In this context, the separate processing of traces belonging to local homogeneous subsurface portions should be preferred (Strobbia and Foti, 2006; Bergamo et al., 2012). As a consequence, detection and location of sharp lateral variations are necessary before processing. In the last decades, several SW based methods have been developed for this purpose.

Park et al. (1998) first proposed the use of SWs to image near surface sharp heterogeneities, which are expected to cause phase velocity and attenuation changes, generation of higher modes and reflected or diffracted waves. The method involves a dynamic linear move out correction in frequency domain followed by the stacking of the corrected shot gather. The anomalous low-velocity zone shows attenuated amplitudes in the results. Hèvin et al. (1998) developed a spectral analysis method to estimate the depth of open cracks in concrete beams, when the location of the crack is a-priori known.

Nasseri-Moghaddam et al. (2005) proposed the Attenuation Analysis of Rayleigh Waves (AARW) to detect shallow underground cavities, later extended to multifold data by Bergamo and Socco (2014). In this last work, the single-fold autospectrum method of Zerwer et al. (2005) was also applied on a seismic data set acquired on a fault system. Adapted versions of the multi-offset phase analysis (MOPA) of Strobbia and Foti (2006) were used by Vignoli and Cassiani (2010) and Vignoli et al. (2011) for the identification of abrupt lateral heterogeneities in the seismic records.

Xia et al. (2007) used diffracted SWs for imaging shallow buried objects and lateral variations, while several authors proposed the use of scattered SWs for the same purpose. These techniques are mainly devoted to the separation of the scattered and incident wavefields, in order to image attributes of the scattered wavefield or for interferometry and inversion purposes (Herman et al.,

2000; Leparoux et al., 2000; Kasilar, 2007; Schwenk et al., 2016; Liu et al., 2017). Hyslop and Stewart (2015) focused on SW reflections and produced reflectivity maps for imaging faults in both numerical and real data.

Reviewing the existing techniques, three tasks can be identified. The first, which is common to almost all methods, is the detection of the heterogeneity and its spatial location. A second task is the estimation of the depth of persistence or embedment of the object. Finally, future perspectives are methods to quantify the contrast in physical and mechanical properties between the object and the background. This paper is focused on the first task, while the other two steps are intentionally left for future work. In particular, the effectiveness in detection and location of sharp lateral variations of four methods (i.e. computation of energy, energy decay exponent, attenuation coefficient and autospectrum) is here compared and discussed using synthetic and real data. These methods were originally introduced in the works of Nasseri-Moghaddam et al. (2005), Zerwer et al. (2005) and Bergamo and Socco (2014). These methods are directly applicable to raw data, without requiring any pre-processing (e.g. filtering, muting, wavefield or SW mode separation) or a-priori knowledge of the investigated subsurface. This enables to carry out systematic analyses with fast, effective and site-independent computations. All the used methods are here updated for multifold data by introducing stacking to improve readability and interpretation of the results. The four methods are firstly applied to 2D synthetic models simulating different shapes, embedment conditions and impedance contrasts with respect to the background. Finally, the methods are validated on two field cases where a-priori knowledge about targets is available.

METHODS

The complete workflow adopted in this study for the different methods is summarized in Appendix A. Hereafter, detailed description of the theoretical basis of each method is provided.

Energy

One of the simplest methods for detection and location of sharp lateral variations is the computation of the energy of the seismic traces acquired along a profile. Energy (E_i) is computed for each receiver i as the sum of the squared amplitudes $A_{f,i}$ at each frequency f, following (Nasseri-Moghaddam et al., 2005):

$$E_i = \sum_f |A_{f,i}|^2 r_i. \qquad (1)$$

To compensate for geometrical spreading, the results are multiplied by a gain function accounting for the distance r_i between source and receiver. For each common shot gather (CSG), resulting E_i values are finally normalized to the maximum E_i recorded along the seismic line and visualized in E-r (energy-distance) plots. Marked energy concentrations or decays are expected at a subvertical discontinuity, as a result of back reflections or energy trapping and amplification within the target. Nasseri-Moghaddam et al. (2005) applied this method to single-fold data to determine the location of underground cavities, observing energy fluctuations in the proximity of the voids. The same method was applied by Bergamo and Socco (2014) to both synthetic and real data of a fault zone, noticing sharp energy decays at the discontinuity location. Colombero et al. (2017) adopted the same method for locating open fractures within a granitic rock mass. Marked energy concentrations at fracture locations were interpreted as the result of back reflections at the discontinuity interfaces. All these previous applications were based on single-fold data. Here, we improve the method by developing its application to multifold data. For each CSG, the energy of each trace is computed following Equation 1. The results are normalized to the maximum for each

shot position. The computation is repeated for all the shots along the seismic line and the results are finally stacked and re-normalized to the maximum of all the shots. The resulting normalized *E-r* plot is used to identify energy concentrations or decays which can be potentially diagnostic of subsurface lateral changes.

Energy decay exponent

The energy decay exponent γ can be defined by the equation (Bergamo and Socco, 2014):

$$\frac{E_{i+1}}{E_i} = \left(\frac{r_{i+1}}{r_i}\right)^{-\gamma}, \qquad (2)$$

where E_{i+1} and E_i are energy values computed at two subsequent receivers i and $i+1$, having offsets r_i and r_{i+1} from the source position. If intrinsic attenuation is disregarded, after recovering geometrical spreading, γ is expected to be zero in a laterally homogeneous medium. If strong deviations from zero are found, these can be interpreted as the result of energy decays (if $\gamma>0$) or concentrations (if $\gamma<0$) induced by back reflections and/or energy trapping within the heterogeneity, coherently to what described for the previous method.

This technique was originally developed and implemented for multifold data by Bergamo and Socco (2014). Taking advantage of data redundancy, the authors obtained a stable estimation of γ values along the seismic profiles. However, the method was tested on a single field case and there are no other applications in literature to evaluate its effectiveness in detection and location of lateral variations. As a consequence, further tests of the method on real and synthetic data are performed in this study. In summary, for each CSG a moving window is shifted along the traces to calculate γ as the slope of the *E-r* plot, in bilogarithmic scale, following (Bergamo and Socco, 2014):

$$log\left(\frac{E_{i+1}}{E_i}\right) = -\gamma\, log\left(\frac{r_{i+1}}{r_i}\right). \qquad (3)$$

For each window, γ values obtained from the different shots are averaged and the related standard deviation is computed, for both positive and negative offsets. Plotting together the averaged results, the presence of sharp lateral variations in the subsurface is expected to generate marked γ oscillations, with opposite trends for positive and negative offsets, caused by the constructive or destructive interaction of the incident and reflected waves at the discontinuity position.

Attenuation coefficient

The evaluation of marked and localized changes of seismic wave attenuation in the subsurface can help to confirm and locate the presence of sharp lateral variations. After compensating for geometrical spreading, the attenuation coefficient α_f can be retrieved from (Bergamo and Socco, 2014):

$$E_{f,i+1} = E_{f,i} e^{-2\alpha_f (r_{i+1} - r_i)}, \qquad (4)$$

where $E_{f,i+1}$ and $E_{f,i}$ are the energy values computed at two subsequent receivers i and $i+1$ (having offsets r_i and r_{i+1} from the source) for each frequency contribution f.

The value of α_f pictures the local attenuation of different frequency components of the propagating wavefield. When a sharp lateral variation is found, the attenuation is strongly influenced by energy reflection at the interface (Xia et al., 2002; Foti, 2004). As for the energy decay exponent, the computation procedure was developed by Bergamo and Socco (2014) on multifold data. For each CSG, a moving window is shifted along the traces to calculate α_f as the slope of the E-r plot (with E in natural logarithmic scale), following:

$$ln\left(\frac{E_{f,i+1}}{E_{f,i}}\right) = -2\alpha_j\left(r_{f+1} - r_i\right). \qquad (5)$$

Given that for location purposes the variations of the parameter along the profile are more interesting than the value itself, to emphasize sudden variations and to enable frequency comparison the obtained α_f are normalized as follows:

$$\overline{\Delta\alpha_{f,w}} = \frac{\overline{\alpha_{f,w}} - (\overline{\alpha_f})}{stdev(\overline{\alpha_f})}, \qquad (6)$$

where $\overline{\alpha_{f,w}}$ is the average attenuation coefficient computed for the window w and for the frequency f, $\overline{\alpha_f}$ is the average attenuation coefficient computed for the frequency f along the whole line and $stdev(\overline{\alpha_f})$ is the related standard deviation value. This procedure is repeated for all the shot gathers along the line and considering both positive and negative offsets. Eventually, these results are averaged over corresponding windows w and frequency ranges f to obtain a single $\overline{\boldsymbol{\Delta\alpha}}$ plot for positive and negative offsets.

Ikeda and Tsuji (2016) applied a similar method on numerical and field data including lithological contrast and fracture presence. The attenuation coefficient was computed considering amplitude instead of energy values (in Equation 4), using data sorted into common midpoint gathers instead of CSGs. Abrupt changes in the attenuation coefficients were clearly observed around fault locations.

In this work, the computation procedure of Bergamo and Socco (2014) is applied to several synthetic and real data to test the applicability on a wide range of cases. Also for this method, to increase the quality of data interpretation, an improvement in the visualization of the results is introduced by stacking the absolute value of the positive ($\overline{\boldsymbol{\Delta\alpha_{POS}}}$) and negative ($\overline{\boldsymbol{\Delta\alpha_{NEG}}}$) plots, following:

$$\overline{\boldsymbol{\Delta\alpha_{STACK}}} = |\overline{\boldsymbol{\Delta\alpha_{POS}}}| + |\overline{\boldsymbol{\Delta\alpha_{NEG}}}|. \qquad (7)$$

Autospectrum

The autospectrum method was originally developed by Zerwer et al. (2005) for the detection of cracks in concrete beams. The autospectral density G_i of a seismic trace $y_i(t)$ can be defined as the sum of the squared real and imaginary parts of the discrete Fourier Transform $Y_i(f)$ of the signal, following (Zerwer et al., 2005):

$$G_i(f) = \{Re[Y_i(f)]\}^2 + \{Im[Y_i(f)]\}^2. \quad (8)$$

As a consequence, computing G_i for a CSG is an alternative way to display the energy content of a seismogram as a function of both frequency and offset. In presence of sharp lateral variations, the same considerations about energy concentration and decay of the previous methods are valid. This technique was applied to the field case study reported in Bergamo and Socco (2014). Seismic energy was found to clearly undergo a decay due to the fault presence, back-reflecting a significant portion of the energy of the incoming wavetrain. Nevertheless, only a qualitative indication of the presence of a lateral change was retrieved from the autospectrum plots, while clear location boundaries and information on the discontinuity shape were not successfully obtained. These limitations are potentially due to the application of the methods to single-fold data. To strengthen the effects of the heterogeneity presence, in this work the procedure is adapted to multifold data. Coherently to the procedures of the other three methods, for each shot location the autospectral density of the traces is computed and geometrical spreading is recovered to remove the effect of the source position on the final plot. The results of different shots are then stacked to improve data readability. Eventually, the normalized plot of the stacked autospectra is used to identify anomalies related to the discontinuity presence.

SYNTHETIC MODELS

To test the effectiveness of the four methods, Finite Element Model simulations (2-D FEM) were implemented in the Structural Mechanics Module of COMSOL Multiphysics® over different models including a localized heterogeneity which represents the detection target. The wave propagation problem is faced in the software using an implicit generalized alpha time-dependent solver. For all models, a half-space configuration (height=1000 m, width=2000 m) with low-reflecting boundaries was chosen, to avoid reflections at the bottom and lateral sides of the domain. In addition, the bottom corner points were fixed to zero displacement. The upper surface was left free. In its central part a synthetic array of 72 geophones (spacing=0.5 m) was simulated, for a total length of 35.5 m (G1 to G72, in Figure 1). Seven sources were located along the seismic line, at the ends (S1 and S7) and within the array (S2 to S6), with a move-up of 12 geophones (Figure 1). A Ricker wavelet centered at 50 Hz was chosen as seismic input for all the simulations. This central frequency was chosen coherently with the highest spectral peak depicted in the field recordings closest to the sledgehammer sources, in order to simulate comparable frequency content.

For all materials, Rayleigh damping was introduced in the models, according to the Q values listed in Table 1. Free triangular meshes were built for all the models, a mesh refinement window of 200x50 m was applied around and below the synthetic array in order to respect a maximum element size lower than one tenth of the minimum wavelength propagating in each model domain, following Mullen and Belytschko (1982). Synthetic CSGs were generated for each model and source location with a time-dependent study in the range 0-0.4 s (coherent with field data recordings) and a sampling frequency of 5 kHz. The peak of the source was centered at 0.1 s, to reproduce the trigger delay in field acquisitions.

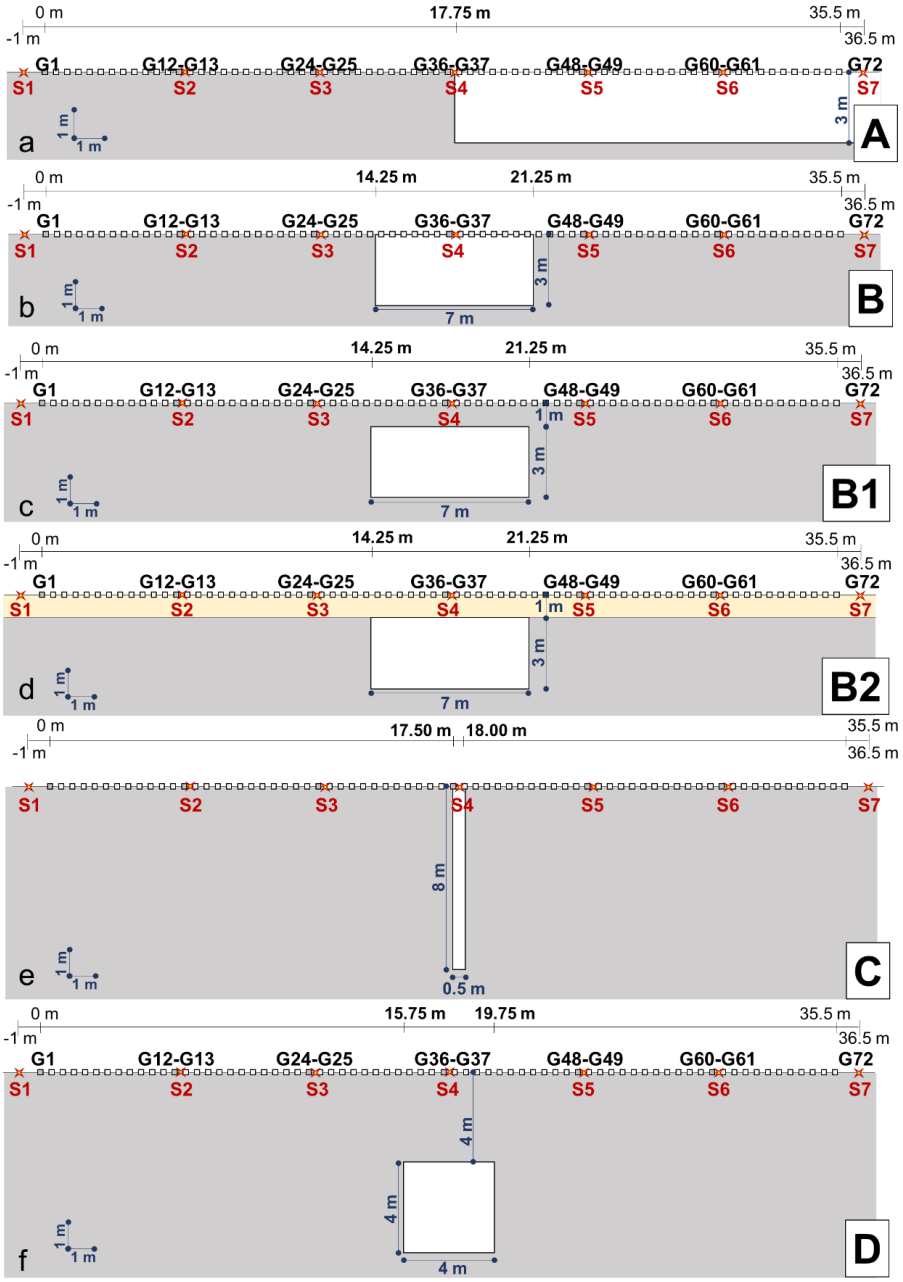

Figure 1. Geometries adopted for the synthetic models, reproducing different shapes of the heterogeneities and embedment conditions. Model parameters are summarized in Table 1 (model name and subscript refer to geometry and material parameters respectively). (a) A_1; (b) B_1, B_2 and B_{2R}; (c) $B1_2$ and $B1_{2R}$; (d) $B2_2$ and $B2_{2R}$; (e) C_3 and C_{3R}; (f) D_3 and D_{3R}. G1 to G72: geophone locations; S1 to S7: shot locations.

The four methods were then directly applied to the synthetic CSGs, without any pre-processing stage. A wide set of geometries and model parameters were used in the simulations with the attempt of testing and comparing the performance of the methods in different and meaningful geological settings. In Figure 1, we show the model geometries used in the simulations. They mimic a sharp lateral discontinuity (e.g. emerging fault or steep slope, A, Figure 1a), a local heterogeneity emerging to the surface (B, Figure 1b) or embedded at 1-m depth in different background conditions (B1 and B2, Figure 1c and Figure 1d), a thin outcropping vertical object (C, Figure 1e) and an embedded equidimensional target (D, Figure 1f). Different model configurations were tested on these geometries; the name of each model corresponds to the adopted geometry, with subscript indicating the material properties summarized in Table 1. Models with different geometry but same material properties were compared (e.g. A_1 and B_1), as well as models having the same geometry but different parameters (e.g. B_1 and B_2). Different embedment conditions were tested for the low-velocity rectangular box of model B_2: homogeneous surrounding material ($B1_2$) and low-velocity layer at the top ($B2_2$). For these three models (B_2, $B1_2$ and $B2_2$), material properties outside and inside the box were also reversed (subscript "R") to additionally account for high-velocity targets (B_{2R}, $B1_{2R}$ and $B2_{2R}$). Analogously, the acoustic impedance contrast between object and background was reversed for models with geometry C, to simulate both a fracture (C_3) and a vein/mineralization (C_{3R}), and D, to reproduce both a cavity (D_3) and a massive ore body ($D3_R$). In these cases, the parameters of the enclosing material were kept constant, while the object was alternatively filled with air (C_3 and D_3) or high-density high-velocity material (C_{3R} and D_{3R}).

Table 1. Physical, mechanical and geometric parameters (P-wave, S-wave, Rayleigh-wave velocity, Poisson's ratio, Density, Quality Factor, depth and length of the heterogeneity) for the materials outside (Mat 1) and inside (Mat 2) the subsurface heterogeneity. For embedded targets, Mat 3 is the material of the overburden. (*) Air velocity and density (at a temperature of approximately 20°C).

Model name	Geometry	Material parameters	Material	V_P [m/s]	V_S [m/s]	V_R [m/s]	ν [-]	ρ [kg/m^3]	Q [-]	Z [m]	L [m]
A_1	**A** (Figure 1a)	**1**	Mat 1	330	175	163	0.3	2200	30	\	\
			Mat 2	200	110	102	0.3	1900	15	3	\
B_1	**B** (Figure 1b)	**1**	Mat 1	330	175	163	0.3	2200	30	\	\
			Mat 2	200	110	102	0.3	1900	15	3	7
B_2	**B** (Figure 1b)	**2**	Mat 1	1040	600	558	0.25	2200	30	\	\
			Mat 2	400	231	215	0.25	2000	20	3	7
B_{2R}	**B** (Figure 1b)	**2R**	Mat 1	400	231	215	0.25	2000	20	3	7
			Mat 2	1040	600	558	0.25	2200	30	\	\
$B1_2$	**B1** (Figure 1c)	**2**	Mat 1	1040	600	558	0.25	2200	30	\	\
			Mat 2	400	231	215	0.25	2000	20	3	7
			Mat 3 (=Mat 1)	*1040*	*600*	*558*	*0.25*	*2200*	*30*	*1*	\
$B1_{2R}$	**B1** (Figure 1c)	**2R**	Mat 1	400	231	215	0.25	2000	20	\	7
			Mat 2	1040	600	558	0.25	2200	30	3	\
			Mat 3 (=Mat 1)	*400*	*231*	*215*	*0.25*	*2000*	*20*	*1*	*7*
$B2_2$	**B2** (Figure 1d)	**2**	Mat 1	1040	600	558	0.25	2200	30	\	\
			Mat 2	400	231	215	0.25	2000	20	3	7
			Mat 3	*260*	*150*	*140*	*0.25*	*1600*	*15*	*1*	\
$B2_{2R}$	**B2** (Figure 1d)	**2R**	Mat 1	400	231	215	0.25	2000	20	\	\
			Mat 2	1040	600	558	0.25	2200	30	3	7
			Mat 3	*260*	*150*	*140*	*0.25*	*1600*	*15*	*1*	\
C_3	**C** (Figure 1e)	**3**	Mat 1	2675	1500	1380	0.27	2570	75	\	\
			Mat 2	340*	\	\	\	1200*	\	8	0.5
C_{3R}	**C** (Figure 1e)	**3R**	Mat 1	2675	1500	1380	0.27	2570	75	\	\
			Mat 2	4795	2935	2700	0.2	2900	75	8	0.5
D_3	**D** (Figure 1f)	**3**	Mat 1	2675	1500	1380	0.27	2570	75	\	\
			Mat 2	340*	\	\	\	1200*	\	4	4
			Mat 3 (=Mat 1)	*2675*	*1500*	*1380*	*0.27*	*2570*	*75*	*4*	\
D_{3R}	**D** (Figure 1f)	**3R**	Mat 1	2675	1500	1380	0.27	2570	75	\	\
			Mat 2	4795	2935	2700	0.2	2900	75	4	4
			Mat 3 (=Mat 1)	*2675*	*1500*	*1380*	*0.27*	*2570*	*75*	*4*	\

SYNTHETIC RESULTS

In the following, we present the results of the application of the four methods to synthetic data. We use models A_1 and B_1 to show the improvement obtained by stacking the information from different shots with respect to single-fold results. For all the other models, only the stacked results are shown (single-shot and single-offset results for all the models are available as online supplementary material). An example test on the stability of the location results in relation to the quality of raw data is discussed in Appendix B, where exemplificative synthetic CSGs are also shown.

For the parameters computed as a function of frequency (attenuation coefficient and autospectrum), the results are plotted with frequency axes from high to low frequencies downwards. This reflects the SW propagation (i.e. high frequencies propagating closer to the surface and low frequencies having higher penetration depth).

Energy

The results of the energy-based method applied to single-shot and multifold data are given for models A_1 and B_1 in Figure 2. Single-shot normalized energy-distance plots are reported in Figure 2a and 2b, while normalized stacked plots of energy are shown in Figure 2c and 2d. In the stacked plots, the position of the target results in a clear anomaly that depict the geometry of object. The stacking significantly reduces the influence of the shot positions, which are indeed clearly visible on the single-shot data.

For all the other models, we show the stacked energy plots only (Figures 3 and 4).

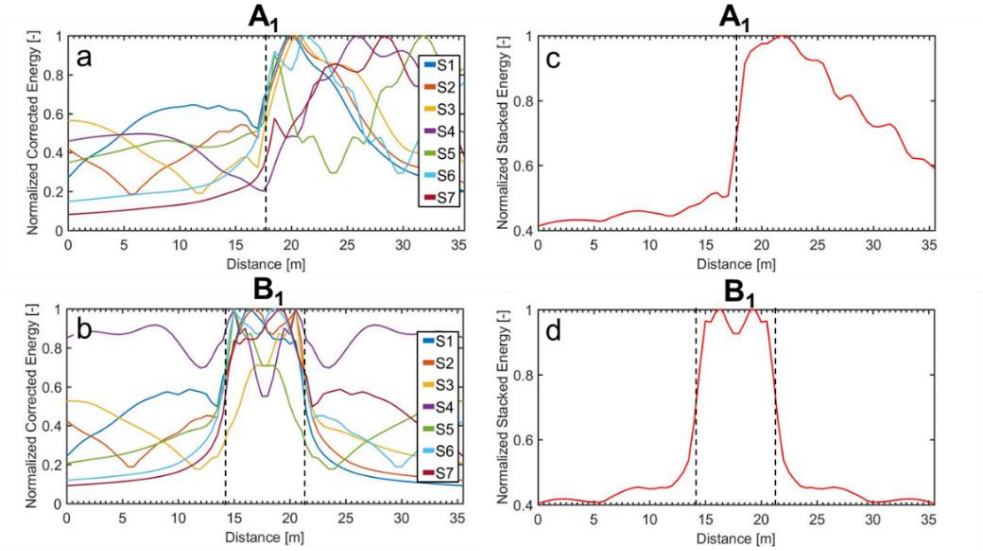

Figure 2. Energy results on (a, c) A_1 and (b, d) B_1. Left column: single-fold results; right column: multifold stacked results. In each section, the vertical dashed lines highlight the real position of the lateral variations.

A clear energy concentration within the low-velocity material is shown for the outcropping bodies (B_1 and B_2, Figure 2d and Figure 3a) and for the box embedded in the homogeneous surrounding material ($B1_2$, Figure 3b). In all these models, the position of the target is marked by a clear energy increase and energy peaks are always observed within the low-velocity material. The box with a 1-m low velocity layer at the top ($B2_2$, Figure 3c) exhibits a different pattern, with energy peaks highlighting the true positions of the box edges. For models having the same geometry but reverse material parameters, we observe an opposite trend with energy drops within the high-velocity heterogeneities. For models B_{2R} and $B1_{2R}$ (Figure 3d and Figure 3e), the normalized energy values outside the bodies are close to 1, and the box edges are located on the descending energy trends. By contrast, $B2_{2R}$ (Figure 3f) is still located by the two peak positions, as observed in the reverse configuration (Figure 3c).

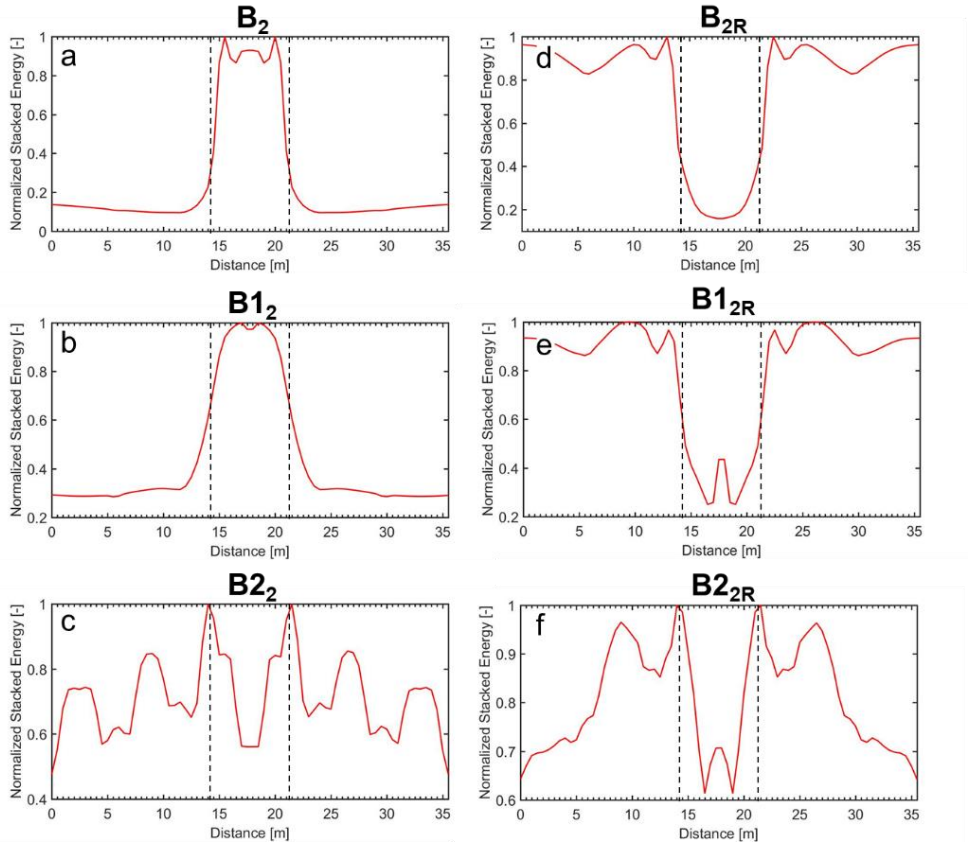

Figure 3. Multifold stacked energy results. (a) B_2; (b) $B1_2$; (c) $B2_2$; (d) B_{2R}; (e) $B1_{2R}$; (f) $B2_{2R}$. In each section, the vertical dashed lines highlight the real position of the lateral variations.

Similar results are also observed over the models with extreme subsurface contrasts and geometries: the fracture (C_3, Figure 4a) and cavity (D_3, Figure 4b) models returned plots coherent to Figure 3a and Figure 3b (B_2 and $B1_2$), with clear energy concentrations in correspondence of the heterogeneity; the high-velocity bodies (C_{3R} and D_{3R}, Figure 4c and Figure 4d) gave opposite results, with a minimum of energy localized over the objects, coherently to Figure 3d and Figure 3e (B_{2R} and $B1_{2R}$), even if the location of these discontinuities is not sharply defined in the plots.

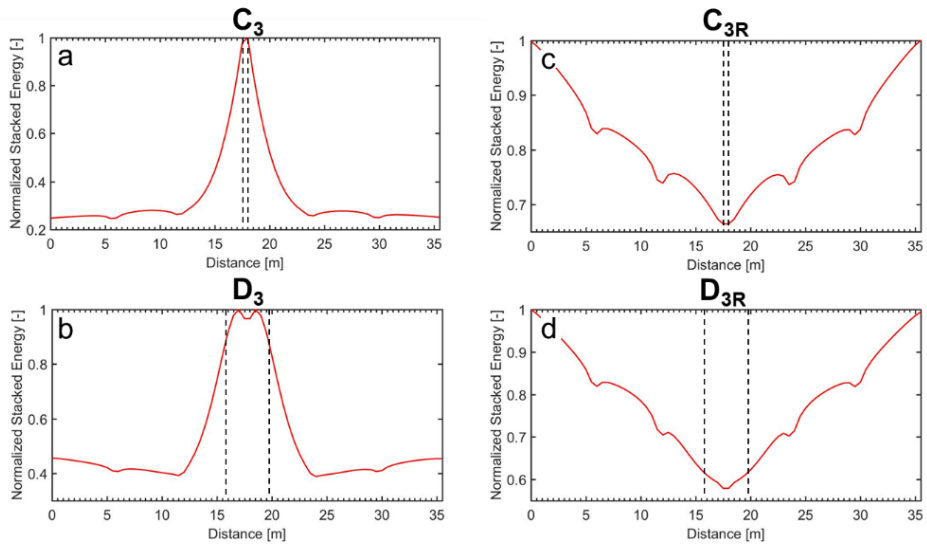

Figure 4. Multifold stacked energy results. (a) C_3; (b) D_3; (c) C_{3R}; (d) D_{3R}. In each section, the vertical dashed lines highlight the real position of the lateral variations.

Energy decay exponent

Energy decay exponent plots are reported in Figures 5, 6 and 7. We plot the values of $-\gamma$ in the results such that maxima correspond to energy concentrations and minima to energy decays. Positive and negative offset results correspond to spatial windows that are located right- and left-side with respect to the shot positions.

In all models, energy concentrations can be observed passing from the high-velocity to the low-velocity material, while energy decays are noted going through the opposite material contrast. Targets in models A_1 and B_1 (Figure 5) are correctly localized by negative and positive $-\gamma$ peaks created by the vertical interfaces between media with different velocities. The best location estimation is obtained as the average of the positions of negative and positive offset peaks.

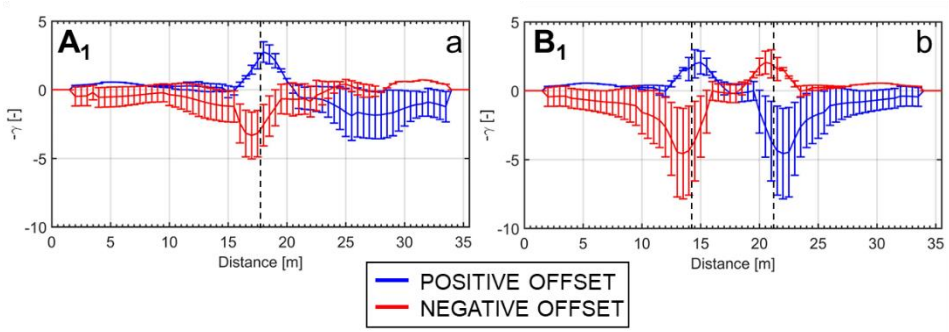

Figure 5. Energy decay exponent results on (a) A_1; (b) B_1. In each section, the vertical dashed lines highlight the real position of the lateral variations.

The amplitude of the peak depends on the contrast between the velocity of target and background. This can be seen by comparing Figure 6a (higher contrast, see Table 1) with Figure 5b, (lower contrast, Table 1). We obtained similar trends for the models with embedded target ($B1_2$ and $B2_2$, Figure 6b and Figure 6c). Even if the location of the boundaries is less sharp, the body edges can be still tentatively localized between the positive and negative offset peaks. The $-\gamma$ anomalies on models $B1_{2R}$ and $B2_{2R}$ (Figure 6e and Figure 6f) appear more marked than in the reverse configurations (Figure 6b and Figure 6c). The results of Figure 7 are coherent with the above observations. Clear energy concentrations are observed before the fracture edges (C_3, Figure 7a) for both positive and negative offsets, while negative peaks are located after them. Model D_3 (embedded cavity) shows a similar trend (Figure 7c). Conversely, only negative γ values are obtained for the vein model (C_{3R}, Figure 7c), even if a slight increase in the curve of positive offsets is found at the vein location. A symmetrical behavior is observed in negative offsets. However, without a-priori knowledge of the target, these results may be insufficient to quantitatively interpret and locate the thin object. Clearer results are obtained on the buried high-impedance body (D_{3R}, Figure 7d).

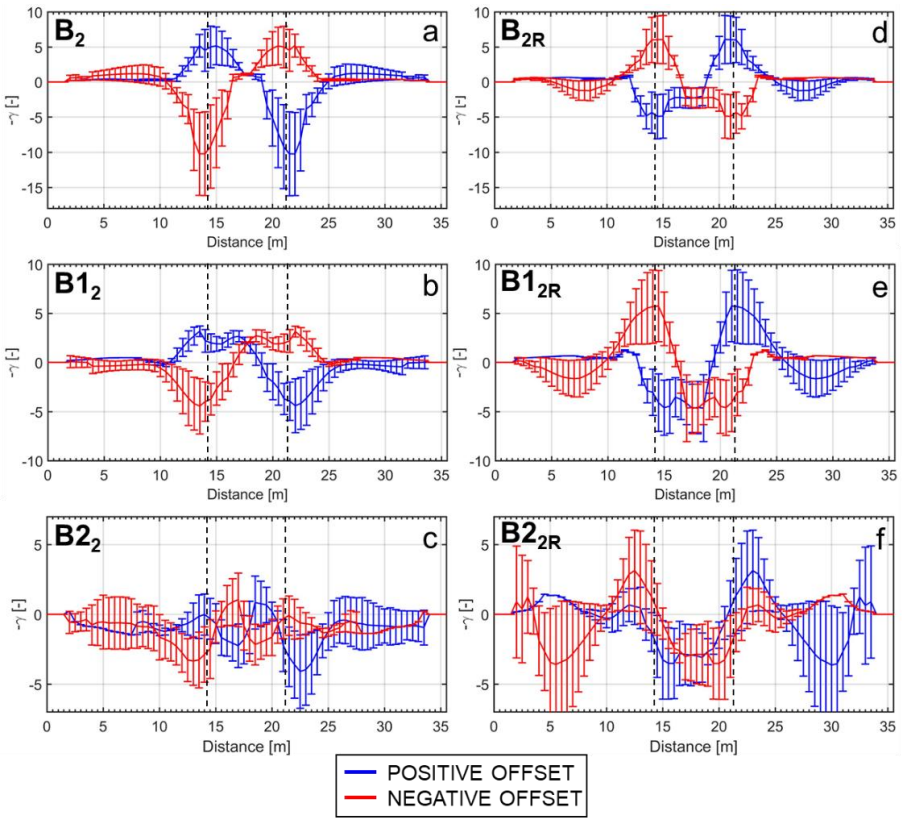

Figure 6. Energy decay exponent results on (a) B_2; (b) $B1_2$; (c) $B2_2$; (d) B_{2R}; (e) $B1_{2R}$; (f) $B2_{2R}$. In each section, the vertical dashed lines highlight the real position of the lateral variations.

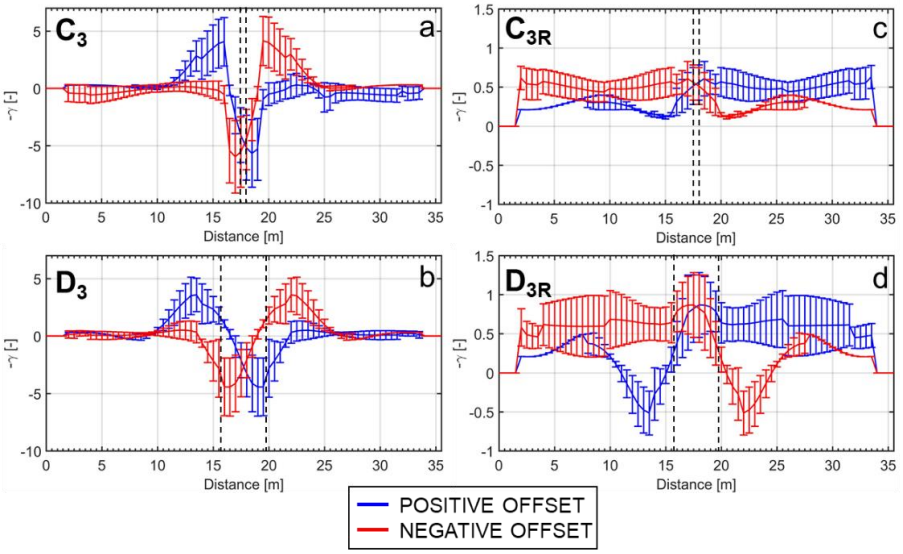

Figure 7. Energy decay exponent results on (a) C_3; (b) D_3; (c) C_{3R}; (d) D_{3R}. In each section, the vertical dashed lines highlight the real position of the lateral variations.

Attenuation coefficient

Attenuation coefficient plots for models A_1 and B_1 are shown in Figure 8. In the left column, positive and negative offset results are separately reported, while in the right column the stacking of the absolute values of the plots on the left is presented. In single-offset results a reduction in attenuation ($\overline{\Delta\alpha} < 0$), reflecting energy concentration, can be observed passing from the high- to the low-velocity material, while an increase in attenuation ($\overline{\Delta\alpha} > 0$), reflecting energy decay, is noted going through the opposite material contrast. The stacked plots offer better imaging potentials, with clearer target location with respect to single-offset plots and overall indication of the target shape. Stacked results are reported in Figure 9 and Figure 10 for the other models.

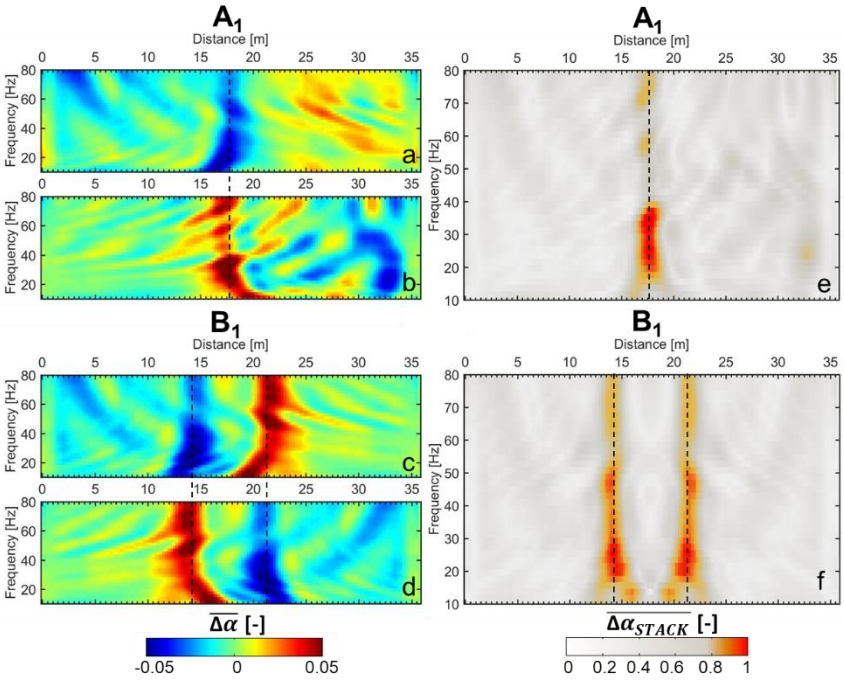

Figure 8. Attenuation coefficient results on (a, b, e) A_1 and (c, d, f) B_1. Left column: separate plots for positive (top) and negative (bottom) offsets. Right column: stacked plot of the single-offset plots (absolute value) on the left. In each section, the vertical dashed lines highlight the real position of the lateral variations.

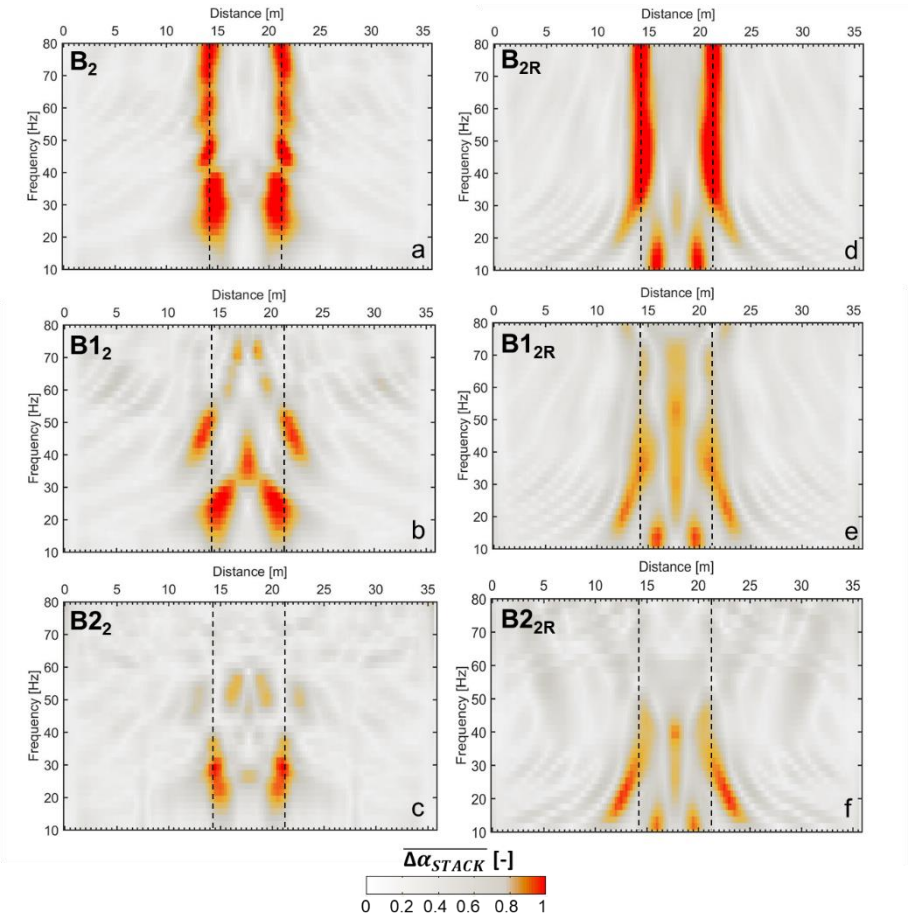

Figure 9. Stacked attenuation coefficient results on (a) B_2; (b) $B1_2$; (c) $B2_2$; (d) B_{2R}; (e) $B1_{2R}$; (f) $B2_{2R}$. In each section, the vertical dashed lines highlight the real position of the lateral variations.

For all models, the highest stacked value of attenuation coefficient variations occurs at the lateral heterogeneity, with the exception of models C_{3R} and D_{3R} where the stiff inclusions are not clearly detected (Figure 10c and Figure 10d). Also for this parameter, the results on the embedded targets are less clear than those on outcropping targets.

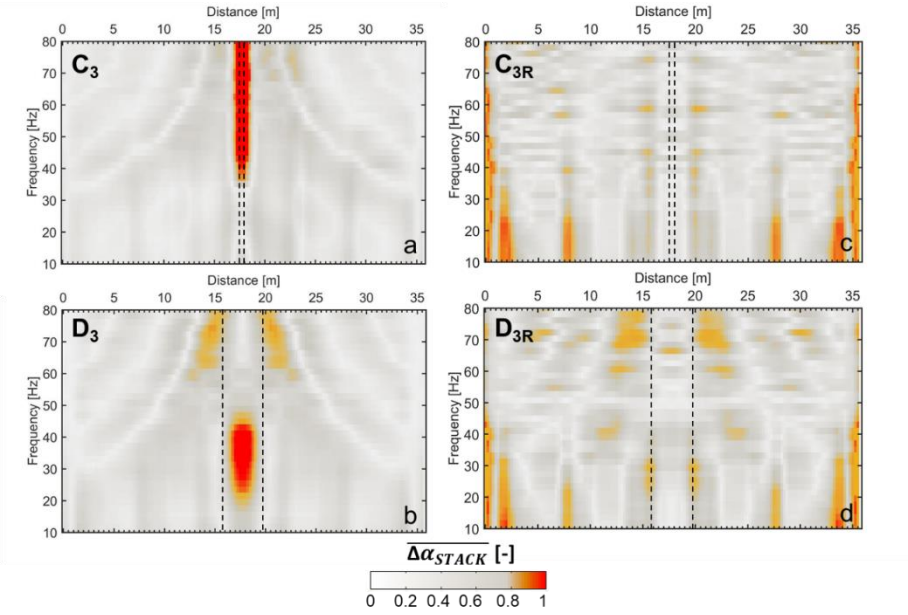

Figure 10. Stacked attenuation coefficient results on (a) C_3; (b) D_3; (c) C_{3R}; (d) D_{3R}. In each section, the vertical dashed lines highlight the real position of the lateral variations.

Autospectrum

We show the autospectrum plots in Figure 11 for models A_1 and B_1, in Figure 12 for the remaining bodies, and in Figure 13 for the fracture and cavity models. Single-fold results are shown only for A_1 and B_1 (Figure 11a and Figure 11b) and for the first shot location (S1, Figure 1). High autospectral values are observed inside the targets when its velocity is lower than the one of the surrounding medium. For all models, multifold results are observed to offer a clearer interpretation of the autospectrum plots, confirming the benefits of data redundancy in sharpening the target aspect. Even if the improvement is only slight for the targets intersecting the ground surface (Figure 11), stacking significantly strengthen the effects of the embedded objects. Unlike previous methods, the box having lower contrast with the enclosing material (B_1 in Figure 11d with respect to B_2 in Figure 12a) seems to produce a clearer evidence.

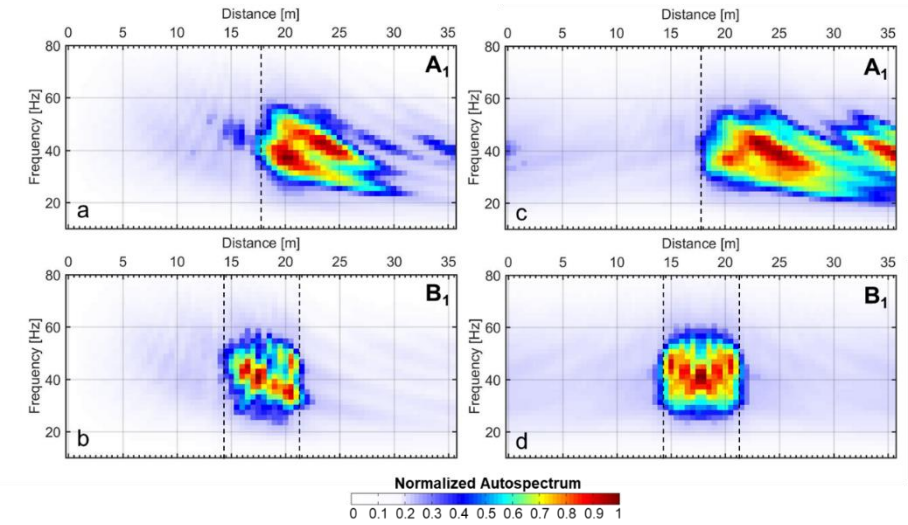

Figure 11. Autospectrum results on (a, c) A_1; (b, d) B_1. Left column: single-fold autospectrum of shot S1. Right column: multifold stacked autospectrum. In each section, the vertical dashed lines highlight the real position of the lateral variations.

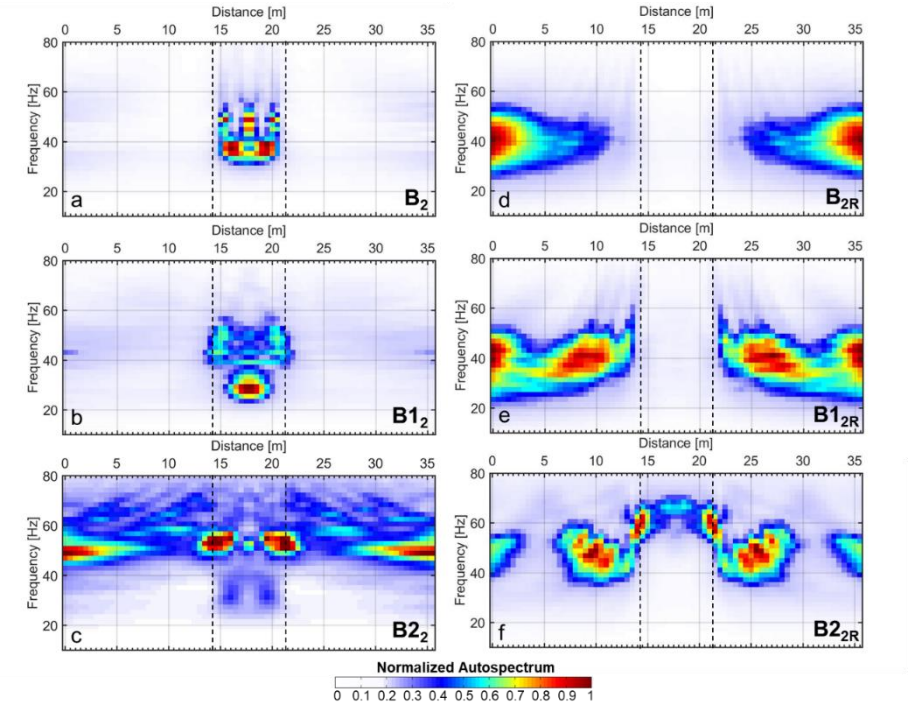

Figure 12. Multifold stacked autospectrum results on (a) B_2; (b) $B1_2$; (c) $B2_2$; (d) B_{2R}; (e) $B1_{2R}$; (f) $B2_{2R}$. In each section, the vertical dashed lines highlight the real position of the lateral variations.

The highest autospectral values are located outside the bodies when acoustic impedance inside the target is higher than the background (right column of Figure 12). This makes the detection of the high-velocity objects a non-straightforward task, especially considering the thin geometry of the vein and the relevant embedment depth of the massive body reported in Figure 13c and Figure 13d. In these configurations, the autospectrum plot can help in target detection, but location and shape are not identified. Conversely, both the fracture and the embedded cavity are correctly located and imagined (Figure 13a and Figure 13b).

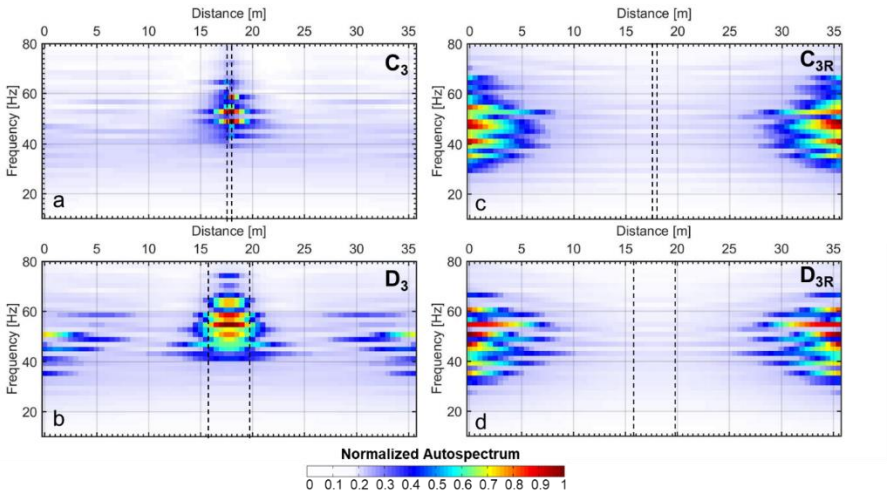

Figure 13. Multifold stacked autospectrum results on (a) C_3; (b) D_3; (c) C_{3R}; (d) D_{3R}. In each section, the vertical dashed lines highlight the real position of the lateral variations.

REAL CASE STUDIES

In the following, we apply the four methods to field datasets acquired at two test sites. The first case study is a shallow low velocity body in a sedimentary sequence, similar to model A_1 for target geometry and material parameters. The second case study is a hard rock site with two large open fractures, similar to model C_3 for the material parameters, but with presence of a shallow overburden and different fracture depths.

CNR test site

Site description

An artificial target was built in an area of CNR (National Research Council) headquarter in Torino, NW Italy (Figure 14a and Figure 14b). The area is flat and characterized by a shallow soil layer overlapping a thick sequence of alluvial deposits of the river plain, mainly composed of gravels with a silty matrix. Within these materials, a square area (length=5 m, width=5 m) was dug down to approximately 2.5 m depth. The void was then filled with loose sand (c in Fig. 14). A seismic line of 72 vertical geophones (4.5 Hz) at 0.3-m spacing was deployed on site (total length=21.3 m) with the sand box in the center of the acquisition line (Figure 14c). Eleven shots (8-kg sledgehammer) were stroke at the line ends and along the array. The first and the last two shots were located at 4 and 2 m respectively from the first and last receiver, while the remaining were evenly spaced along the seismic line. Traces were recorded at 0.125-ms sampling rate, with a trigger delay of 0.1 s, for a total acquisition time of 0.512 s. An exemplificative shot gather (S1) is shown in Figure 14d.

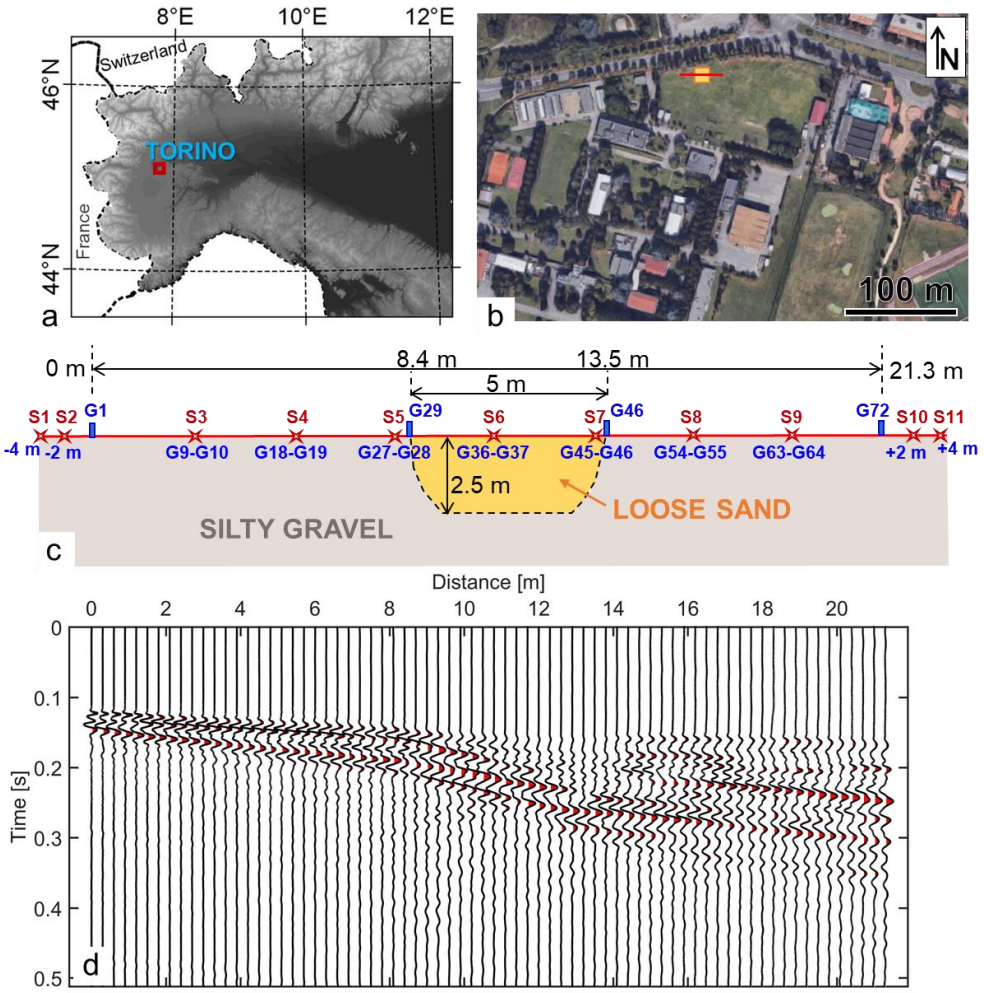

Figure 14. CNR test site. (a) Geographic location. (b) Aerial view of the site with location of the sand box (yellow square) and the seismic array (red line). (c) Geometry of the target and seismic layout. G1 to G72: geophone locations; S1 to S11: shot locations. (d) Common shot gather for S1.

Results

The results of the four methods are summarized in Figure 15. The normalized stacked energy plot, obtained from the 11 shots along the line, is shown in Figure 15a. Clear energy concentration is found inside the sand body, in agreement with the synthetic results (e.g. B_1, Figure 2d). In both plots, the target edges are located at the steep increase and decrease of the normalized energy values. Energy decay exponent results are reported in Figure 15b. As observed for the

synthetic models (e.g. B_1, Figure 6a), the peaks in $-\gamma$ values correctly detect and localize the position of the sand body. For both positive and negative offsets, energy concentration is found entering the low velocity body, while energy decay is recorded exiting from it. The attenuation coefficient and autospectrum results succeed as well in the location of the target, with a clear and sharp imaging in the stacked plot (Figure 15c and Figure 15d). Comparable results are obtained for the synthetic model B_1 (Figure 8f and Figure 11d).

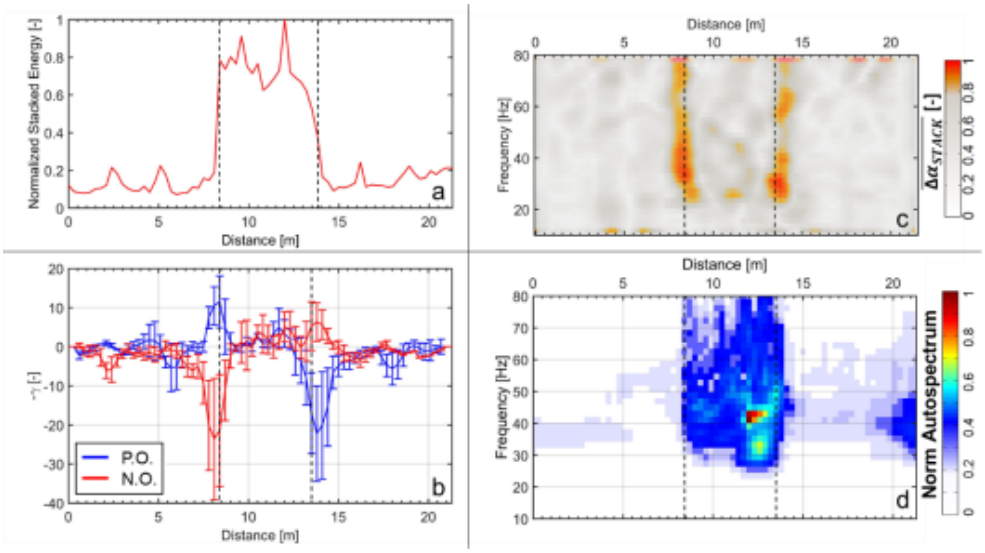

Figure 15. CNR results. (a) Multifold stacked energy-distance plot. (b) Energy decay exponent results. (c) Stacked attenuation coefficient results. (d) Multifold stacked autospectrum plot. In each section, the vertical dashed lines highlight the approximate real position of the box edges.

Madonna del Sasso

Site description

The unstable cliff of Madonna del Sasso (NW Italy, Figure 16a) is a granitic rock mass with five main fractures (F1 to $F4_1$ and $F4_2$, in Figure 16b and Figure 16c) potentially isolating two unstable rock prisms at the top of the cliff. Several geophysical surveys were carried out on site. P- and S-wave cross-hole tomography was used to image fractures $F4_1$ and $F4_2$ (Colombero

et al., 2016). Despite two low-velocity zones were identified in the tomographic results, the low ray coverage and the resulting smooth tomograms did not allow fracture locations and boundaries to be shapely delineated. The single-fold energy method was applied on a surface seismic line in Colombero et al. (2017).

In this work, we apply all the four methods to the same dataset. Data were acquired with 48 vertical (4.5 Hz) geophones at a spacing of 0.75 m, covering the longest available line on the top of the cliff (G1 to G48, Figure 16c and Figure 16d). A total of 13 shot positions (8-kg sledgehammer) were stroke at the line ends and along the array. The first and last source positions were located at 1-m distance from the first and last geophones (S1 and S13, Figure 16d). S1 CSG is shown in Figure 16e. According to the previous studies, the two fractures are supposed to cross the seismic line almost perpendicularly at a distance of approximately 14.1 m ($F4_2$) and 21.6 m ($F4_1$) with subvertical dip. Below a thin soil cover, they are expected to be open, as demonstrated by past episodes of collapse of the cover. Their width is estimated in approximately 0.5 m, with a depth of several meters from the ground surface (16 m±2 m for $F4_1$ and 8 m±2 m for $F4_2$, according to the results of Colombero et al., 2017).

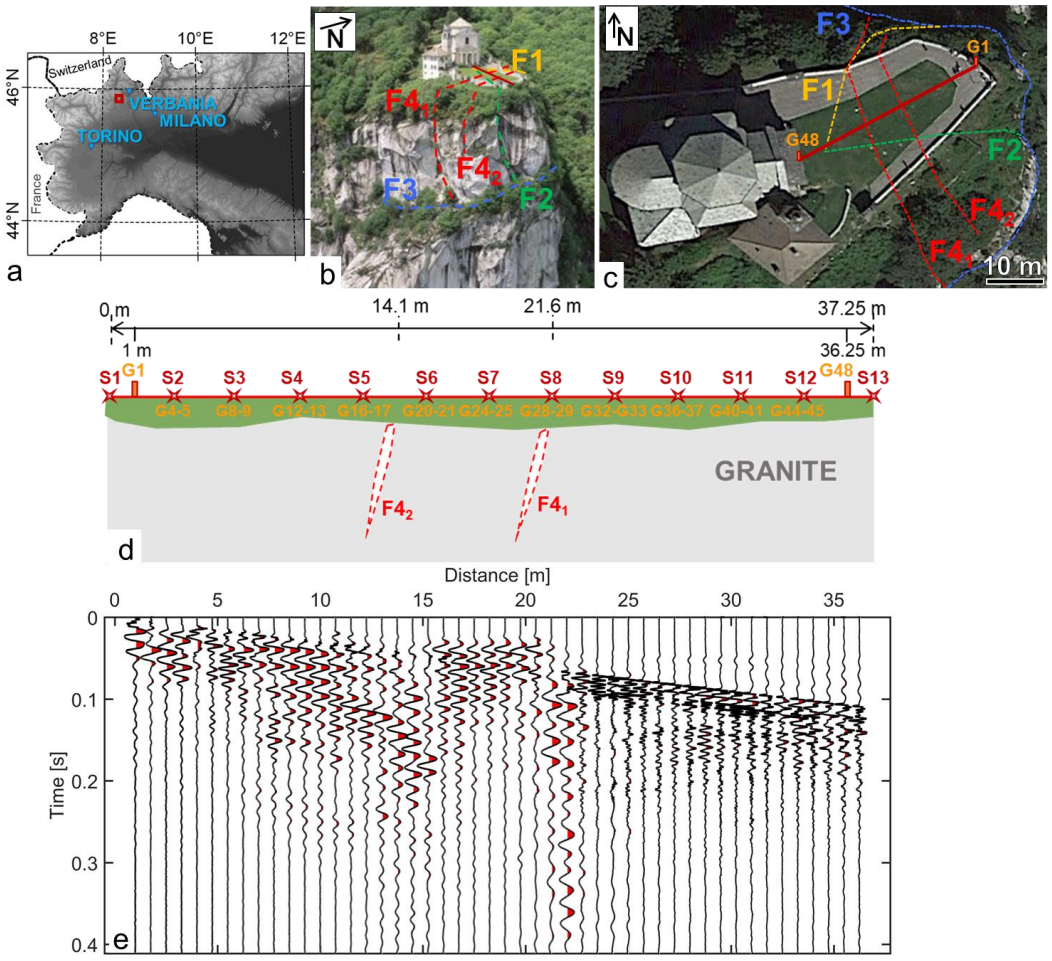

Figure 16. Madonna del Sasso test site. (a) Geographic location. (b, c) Aerial views of the site with location of the main fractures (F1 to F4, dashed lines) and seismic array (red continuous line). (d) Geometry of the seismic layout and fracture locations. G1 to G48: geophone locations; S1 to S13: shot locations. (e) Common shot gather for S1.

Results

The results of the four methods are summarized in Figure 17. The stacked normalized energy-distance plot is reported in Figure 17a. Also in this case, clear energy concentrations are noticed at the fracture locations, in agreement with the synthetic results on the single fracture C_3 (Figure 4a). The cross points between positive and negative peaks of the energy decay exponent

(Figure 17b) are located in proximity of the fractures, as in the synthetic results obtained on model C_3 (Figure 7a). Nevertheless, the real data are not as clear the synthetic results. Marked peaks are found on the two sides of the fractures in the attenuation coefficient results (Figure 17c), differently from the synthetic results on the single open fracture highlighting a maximum inside the target (Figure 10a). An additional maximum is found between 33-35 m at high frequencies. This anomaly can be noticed also in the energy results (Figure 17a), but does not appear in the energy decay exponent (Figure 17b) and in the stacked autospectrum plot (Figure 17d). The autospectrum produces a sharp image of the investigated fractures in agreement with synthetic data (Figure 13a).

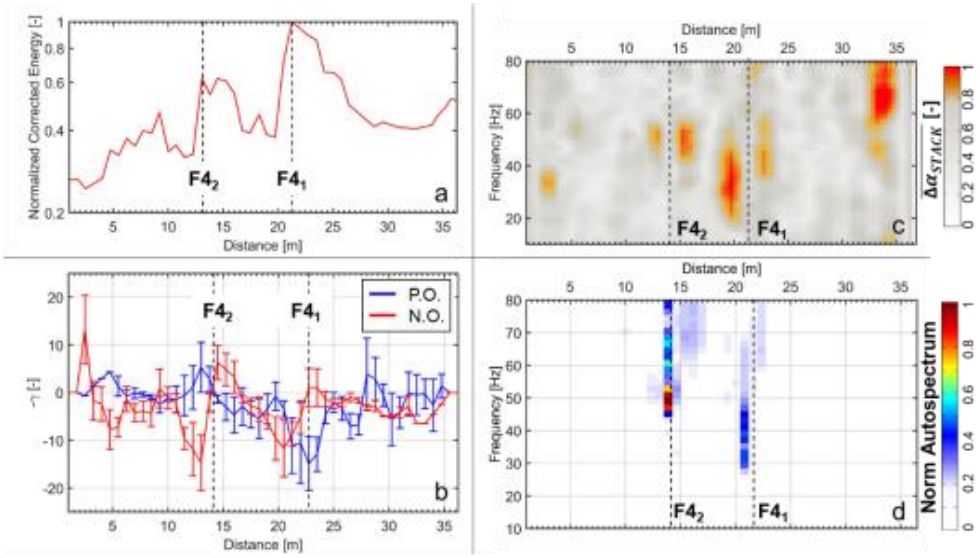

Figure 17. Madonna del Sasso results. (a) Multifold stacked energy-distance plot. (b) Energy decay exponent results. (c) Stacked attenuation coefficient results. (d) Multifold stacked autospectrum plot. In each section, the vertical dashed lines highlight the approximate real position of fractures.

DISCUSSION

To compare the effectiveness of the four methods in detecting and locating sharp lateral variations, clear criteria for the quantitative interpretation of the results were needed. We chose the horizontal gradient of the four computed parameters to highlight the strongest lateral variations and consequently provide clear common location criteria. The gradient computation along the seismic line was straightforward for energy and energy decay exponent curves. In order to provide comparable results for the 2D plots of the other two methods, the attenuation coefficient and autospectral values at different frequencies were summed along the frequency axis to obtain a single value for each receiver location. The horizontal gradient was then computed on the resulting vectors.

Interpretation of synthetic and field results

We show the plots of horizontal gradients (normalized absolute values) in Figure 18 for models A_1 and B_1, Figure 19 for all the other box configurations (B2, $B1_2$, $B2_2$, $B2_R$, $B1_{2R}$, $B2_{2R}$), and Figure 20 for the remaining synthetic models (C3, D3, $C3_R$, $D3_R$). The results on the two real case studies are reported in Figure 21.

In the synthetic results, the sharp lateral variations were generally located on the steep energy increases and decreases. We consequently chose the maxima in the absolute value of energy gradients as representative locations of the lateral variations for this method. The same criterion was adopted for the absolute value of the autospectrum gradients. For the energy decay exponent, considering that the sharp lateral variations were observed to be approximately located between the location of minima and maxima of positive and negative offsets, the absolute value of the horizontal gradient was computed for both offsets. The local minimum between two gradient peaks was then selected as representative of the lateral variation location for each offset curve. These

minima are located on the two side of the discontinuity for opposite offsets, coherently with $-\gamma$ results. The average value of positive and negative offset gradient minima was consequently chosen as representative point for the discontinuity location. A similar criterion was followed for the attenuation coefficient results. Given that maxima in the stacked attenuation plots were generally observed at the edges of the heterogeneities, the local minimum between two gradient peaks was selected as location of the lateral variation.

Errors in the location obtained following these criteria for all the simulated and real heterogeneities are summarized in Table 3. In general, energy gradient maxima were found to perform well in the location of the outcropping anomalies having lower velocity than the surrounding material (A_1, B_1, B_2 and C_3 in Figure 18, Figure 19a and Figure 20a), with errors lower than the geophone spacing (0.5 m). Comparing results are recorded on the embedded box $B1_2$ and $B1_{2R}$ (Figure 19b and Figure 19e), with maximum errors of ±0.25 m from the real locations. Higher errors were found for the embedded boxes with a low velocity layer at the top, i.e. $B2_2$ (±0.75 m; Figure 19c) and $B2_{2R}$ (±1.50 m; Figure 19f). For these models it was already observed in the energy results of Figure 3c and Figure 3f that the exact location of the targets corresponds to the energy peaks, and not the increasing and decreasing energy ramps. The vein and the massive ore body in models C_{3R} and D_{3R} could not be located following the same criterion (Figure 20c and Figure 20d). Even if local maxima in the energy gradient are present close to these discontinuities, higher peaks are observed towards the line ends. These complex patterns make the location almost impossible on energy gradient curves, while the original energy plots (Figure 4c and Figure 4d) gave at least an indication of the presence of a body with high acoustic impedance in the center of the profiles.

The peaks in the energy gradient are also found to locate the edges of the sand box for CNR test site (Figure 21a), with errors comparable to the geophone spacing adopted on site (0.3 m). The

fractures of Madonna del Sasso are located with errors generally double than the adopted 0.75-m geophone spacing (Figure 21b). Similar considerations apply to the autospectrum gradients of both synthetic and real data. The highest errors are recorded for model $B2_2$ (±0.75 m; Figure 19c). For this model, local maxima closer to the real edge locations are present in the gradient results.

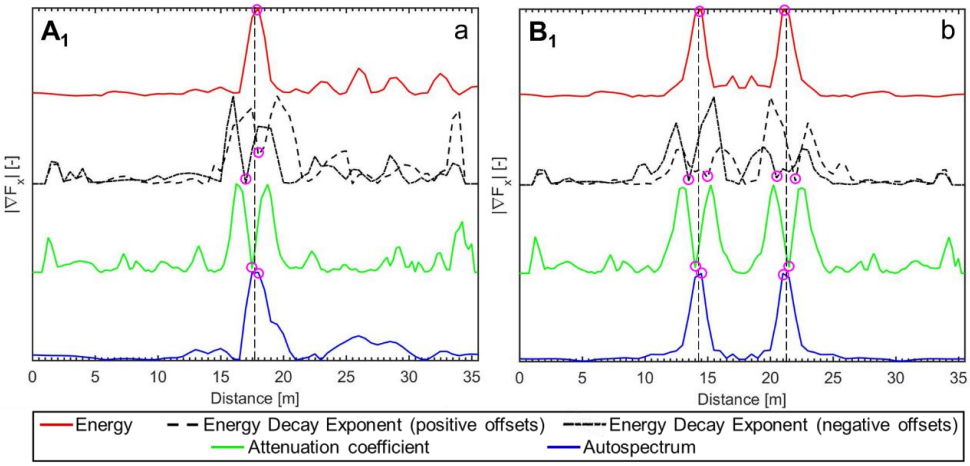

Figure 18. Normalized absolute value of the horizontal gradients of the four parameters on (a) A_1 and (b) B_1 synthetic models: energy (in red), energy decay exponent (in black; dashed line: positive offsets; dash-dotted line: negative offsets), attenuation coefficient (in green), autospectrum (in blue). In each section, the vertical dashed lines mark the real position of the lateral variations, while the magenta circles highlight the locations of the lateral variations, according to the criteria described in the text.

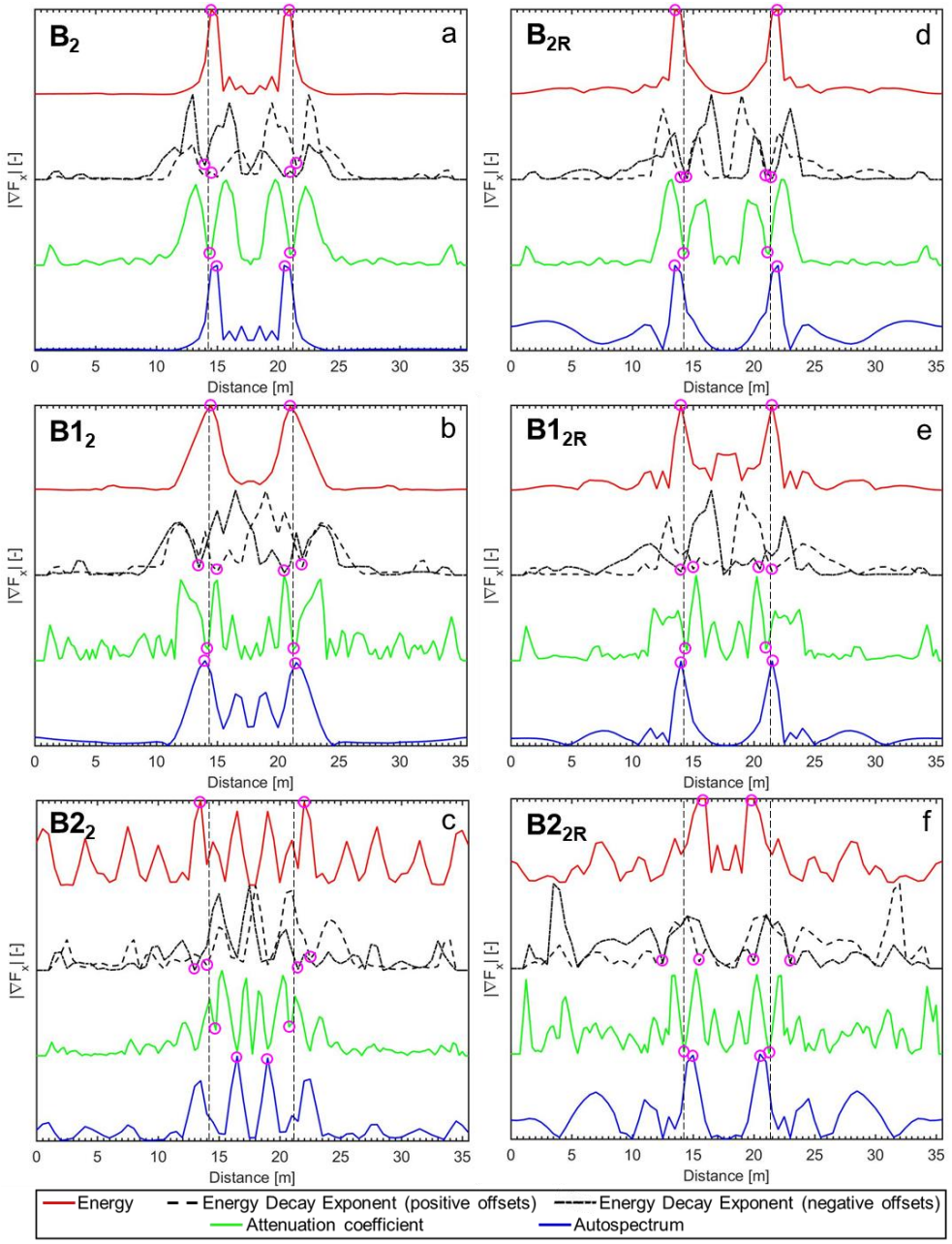

Figure 19. Normalized absolute value of the horizontal gradients of the four parameters on (a) B_2, (b) $B1_2$, (c) $B2_2$, (d) B_{2R}, (e) $B1_{2R}$, (f) $B2_{2R}$ synthetic models: energy (in red), energy decay exponent (in black; dashed line: positive offsets; dash-dotted line: negative offsets), attenuation coefficient (in green), autospectrum (in blue). In each section, the vertical dashed lines mark the real position of the lateral variations, while the magenta circles highlight the locations of the lateral variations, according to the criteria described in the text.

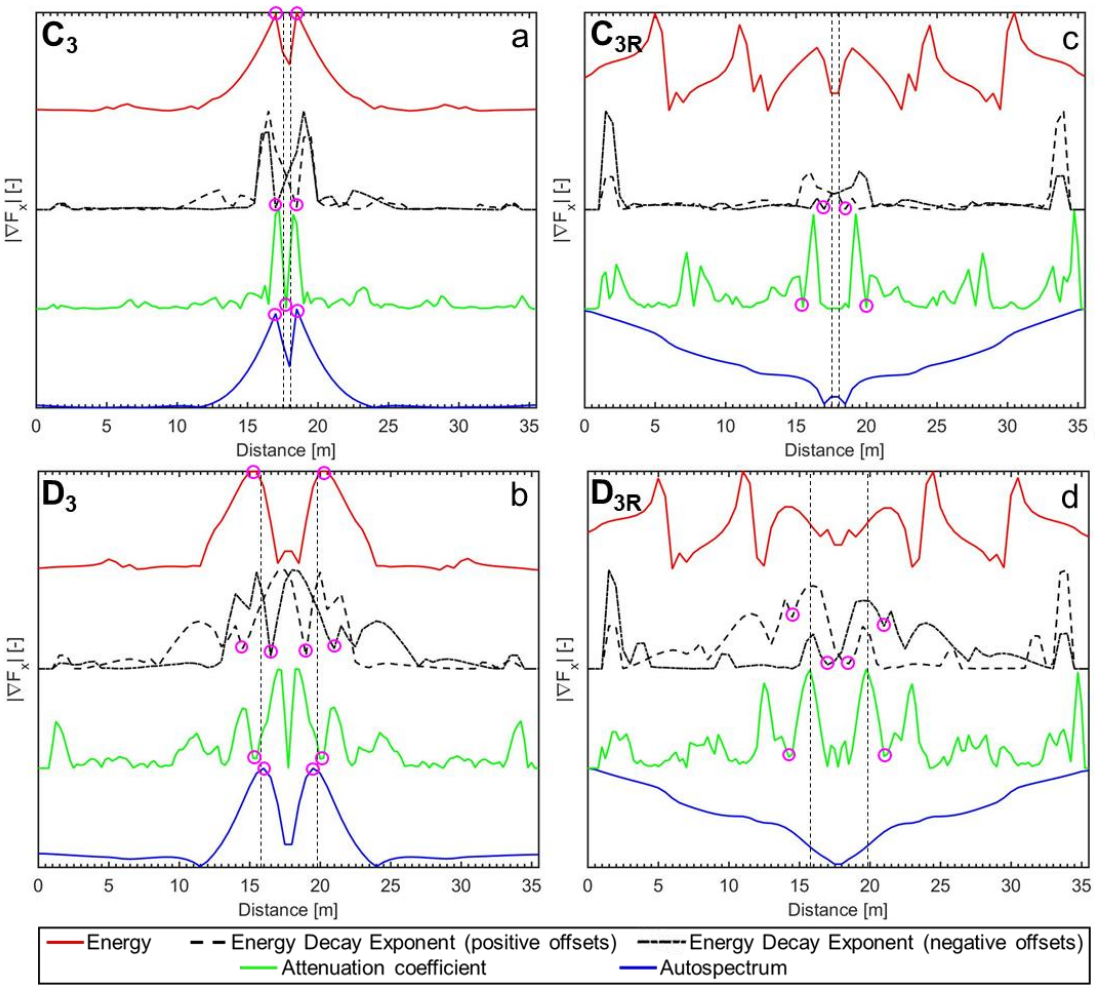

Figure 20. Normalized absolute value of the horizontal gradients of the four parameters on (a) C_3; (b) D_3; (c) C_{3R}; (d) D_{3R}: energy (in red), energy decay exponent (in black; dashed line: positive offsets; dash-dotted line: negative offsets), attenuation coefficient (in green), autospectrum (in blue). In each section, the vertical dashed lines mark the real position of the lateral variations, while the magenta circles highlight the locations of the lateral variations, according to the criteria described in the text.

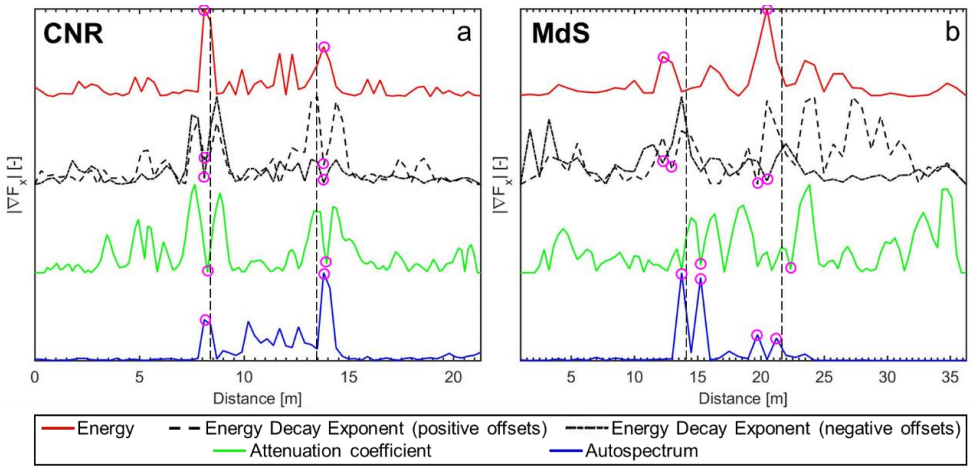

Figure 21. Normalized absolute value of the horizontal gradients of the four parameters on (a) CNR test site; (b) Madonna del Sasso cliff: energy (in red), energy decay exponent (in black; dashed line: positive offsets; dash-dotted line: negative offsets), attenuation coefficient (in green), autospectrum (in blue). In each section, the vertical dashed lines mark the real position of the lateral variations, while the magenta circles highlight the locations of the lateral variations, according to the criteria described in the text.

Table 2. Location errors, reported as the distance between the real position (estimated from previous works for the real case studies) and the location retrieved from the gradient of the four parameters. LE: left edge and RE: right edge of the box models. For Madonna del Sasso (MdS) site, LE and RE refer to the average locations of fractures $F4_2$ and $F4_1$ respectively.

Model/	**E**		**γ**		**α**		**Autospectrum**	
Case study	LE [m]	RE [m]	LE [m]	RE [m]	LE [m]	RE [m]	LE [m]	RE [m]
A_1	-0.25		0.25		0.25		0.00	
B_1	-0.25	0.25	0.00	0.00	0.25	-0.25	-0.25	0.25
B_2	-0.25	0.25	-0.25	-0.25	-0.25	0.25	-0.75	0.75
B_{2R}	0.75	-0.75	0.00	0.00	0.00	0.00	0.75	-0.75
$B1_2$	-0.25	0.25	0.00	0.00	0.00	0.00	0.25	-0.25
$B1_{2R}$	0.25	-0.25	-0.25	0.25	-0.25	0.25	0.25	-0.25
$B2_2$	0.75	-0.75	0.75	-0.75	-0.50	0.50	-2.25	2.25
$B2_{2R}$	-1.50	1.50	0.25	-0.25	0.00	0.00	-0.75	0.75
C_3	0.50	-0.50	0.50	-0.50	-0.25	0.25	0.50	-0.50
C_{3R}	?	?	0.50	-0.50	2.00	-2.00	?	?
D_3	0.25	-0.25	0.25	-0.25	0.25	-0.25	-0.25	0.25
D_{3R}	?	?	0.00	0.00	1.25	-1.25	?	?
CNR	0.30	-0.30	0.30	-0.30	0.15	-0.45	0.30	-0.30
MdS	1.60	1.10	1.48	1.48	-1.15	-0.78	-0.40	1.10

The picking of the lateral variation locations on the energy decay exponent gradient plots is clear and well-fitting with the real locations for the outcropping targets A_1, B_1, B_2 and B_{2R} (Figure 18, Figure 19a and Figure 19d), independently from the material contrast. Boxes embedded in the homogeneous background ($B1_2$ and $B1_{2R}$) also showed clear gradient curves and location errors lower than the adopted geophone spacing (Figure 19b and Figure 19e). The results on the box with low-velocity overburden (Figure 19c and Figure 19f) are however more complex, gradient curves on $B2_{2R}$ exhibit maxima close to the line ends which could lead to erroneous picking without a comparison with the other methods. Despite energy and autospectrum results, an estimation of the vein and massive body locations in models C_{3R} and D_{3R} is possible with the energy decay exponent (Figure 20c and Figure 20d). Gradient spikes are however observed at the

line ends. Comparable results are obtained with the attenuation coefficient gradients for both synthetic and real data. Also for this method, it is possible to retrieve an estimation of the vein and massive body locations, even if with errors higher than 1 m.

Despite these limitations, the evaluation of the horizontal gradients can help in quantitatively compare the results of the four methods and in the coherent selection of the discontinuity locations. However, when the obtained gradient curves become unclear and noisy due to the complexity of the subsurface conditions, an approximate location estimation based on the plots shown in the results of each methods should be preferred. It must be additionally noticed that the errors in the location (Table 3) strictly depend on the receiver spacing adopted in both synthetic and real case studies. With higher receiver spacing, the uncertainty in the location would proportionally increase.

We observed poor location results for anomalies having higher acoustic impedance than the surrounding material. This weakness probably depends on the strength of the acoustic impedance contrast between the two media (e.g. higher on B_{2R} than on C_{3R}), on the geometry of the anomaly (e.g. C_{3R} is extremely thin if compared with B_{2R}) and on the embedment depth (e.g. D_{3R} vs $B1_{2R}$). In these cases, the joint computation of all the four methods can however help to detect the anomaly presence.

Results of CNR field data were found in good agreement with similar synthetic data (i.e. model B_1), while major differences were observed between Madonna del Sasso and model C_3 (single fracture). For the field case, the presence of two discontinuities interfering in a short space and of a shallow overburden, the unknown geometry and filling of fractures at depth and the possible heterogeneity in the background material (due to additional fracturing and weathering) are all factors which probably contributed to the observed discrepancies with synthetic data.

Comparison with single-fold and single-offset results

The advantage of introducing stacking of CSG results in energy and autospectrum computations and of positive and negative offset plots for attenuation coefficient is already clear by visual comparison of single-fold/offset plots and multifold results (e.g. Figure 2, Figure 8, Figure 11 and online supplementary material). However, it was quantitatively analyzed with the same gradient criteria. As a synthetic example, the gradient of energy and autospectrum for a single shot gather (S1) are shown in comparison with the gradients of multifold results for model A_1 (Figure 22a and Figure 22b) and model B_1 (Figure 22d and Figure 22e). For the same models, the gradients of positive and negative offset results for attenuation coefficient are reported in comparison with the gradient of the stacked plots in Figure 22c and Figure 22f. Even if the errors in target locations are similar for single and stacked results, stacking strengthens and sharpens the effect of the anomaly in all plots. The peaks linked to the target are sharpened and their amplitude is increased, while the amplitude of secondary peaks (not related to the target) is decreased in the stacked results (e.g. secondary peaks in Figure 22a or high positive and negative offset peaks at the ends of the profile in Figure 22c and Figure 22f). This may reduce the uncertainty in the interpretation of field data with unknown target number and features.

In Figure 23 we show similar comparisons for the field data of CNR and Madonna del Sasso. In both cases, data interpretation based on the peak positions in the single-fold results of energy and autospectrum would lead to erroneous detection and location estimations.

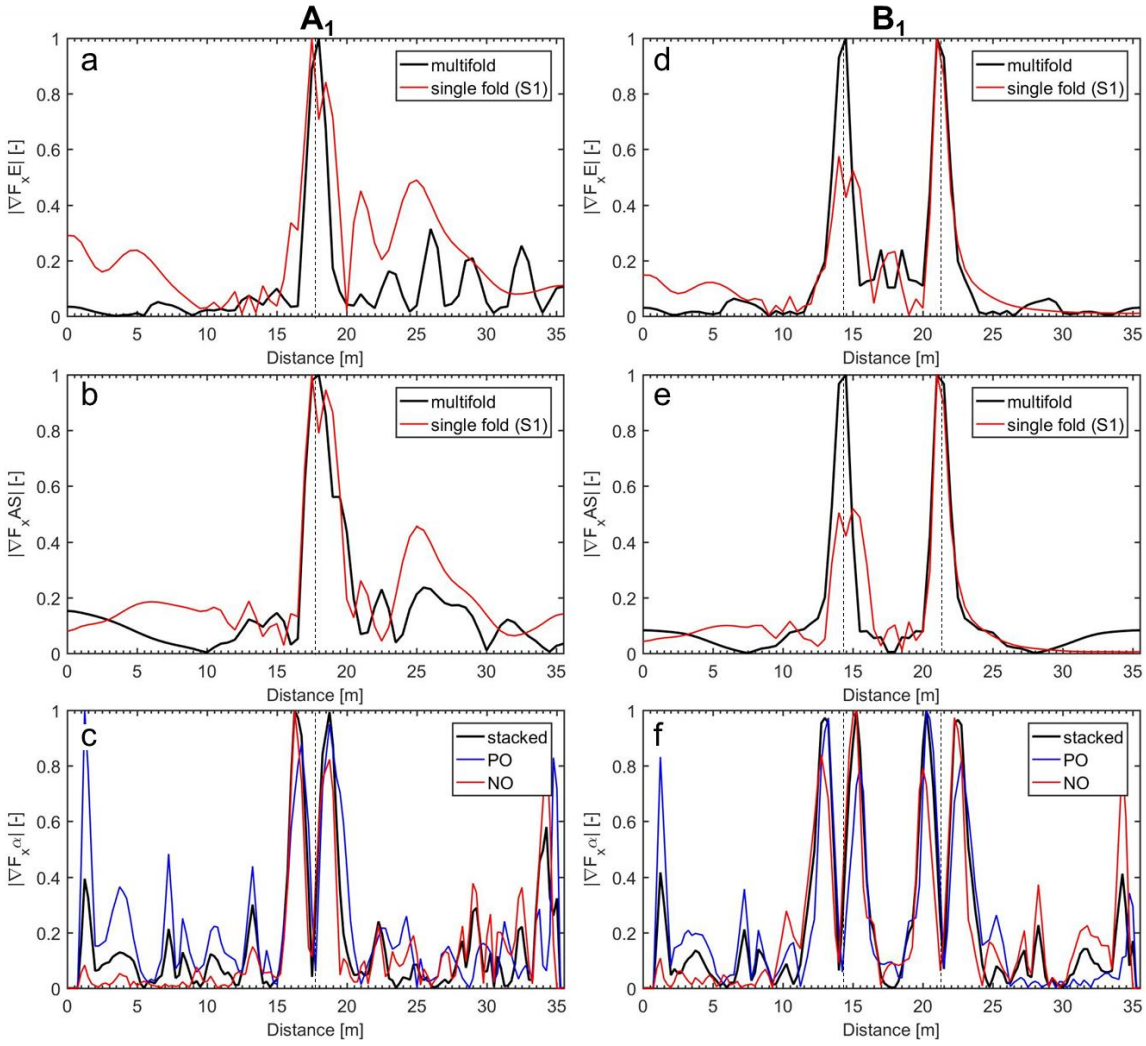

Figure 22. Comparison of single-fold/offset and stacked results for the synthetic model (a-c) A_1 and (d-f) B_1. (a, d) S1 and multifold stacked normalized energy gradients. (b, e) S1 and multifold stacked normalized autospectrum gradients. (c, f) Attenuation coefficient normalized gradients for positive offset, negative offset and stacked results.

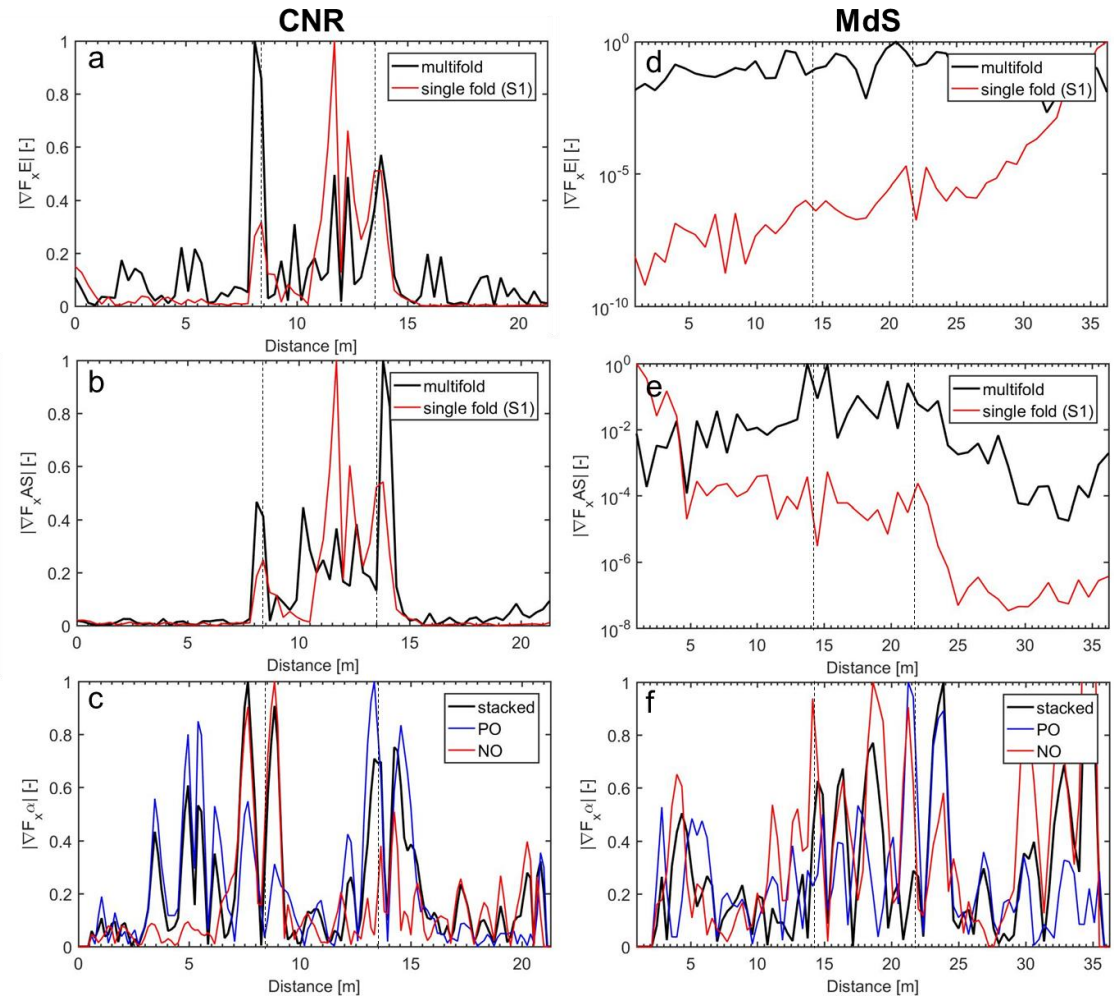

Figure 23. Comparison of single-fold/offset and stacked results for the field data (a-c) CNR and (d-f) Madonna del Sasso. (a, d) S1 and multifold stacked normalized energy gradients. (b, e) S1 and multifold stacked normalized autospectrum gradients. (c, f) Attenuation coefficient normalized gradients for positive offset (PO), negative offset (NO) and stacked results. In (d) and (e) the y-axis is in logarithmic scale to intensify the small fluctuations of single-fold gradients.

CONCLUSIONS

Sharp lateral variations in the shallow subsurface can be either a target of investigation for near-surface seismic surveys or an issue for local 1D model reconstructions of the subsurface in SW processing. Reliable, effective and computationally fast methods are consequently required to recognize their presence. These methods can use SWs propagation, given their strong interaction with local sub-vertical discontinuities and lower attenuation with respect to body waves. The tasks explored in this work were the detection and location of the sharp lateral variations. Four SW-based methods were chosen, for their fast and effective workflows, not requiring any pre-processing of raw data, wavefield or mode separations. The proposed methods were adapted to multifold data to strengthen the effects of the discontinuity and improve reliability in the interpretation of the results. The horizontal gradient of the four parameters was analyzed to establish objective and quantitative criteria for target location.

All the tested methods showed good ability to detect and locate lateral variations having acoustic impedance lower than the surrounding material on synthetic data with errors lower than 1-2 m, for the adopted receiver spacing. These results were confirmed on two real case studies having the same configuration (low acoustic impedance targets). More difficulties were encountered in locating targets with higher acoustic impedance than the surrounding material. In this configuration, weak contrasts in acoustic impedance, high embedment depths and small dimensions of the discontinuity can prevent from a precise location of the targets. The strength of the proposed methods lies in: i) absence of any pre-processing, ii) robustness of the results, also in case of noisy data. The complete workflow, from the upload of the seismic records to the final results, over a commercial laptop requires less than 5 minutes (for 10 to 15 CSGs of 48-72

receivers), making this approach a potential method for fast object identification directly in the field.

In all the simulated conditions, sharp lateral variations were considered as vertical interfaces, but additional simulations on dipping interfaces showed analogous detection potentialities. However, the evaluation of location errors due to the presence of dipping interfaces is left for future work. In addition, the sensitivity of the four techniques to variable depths of the target and the potentiality in indirect depth estimation from the frequency-dependent methods (attenuation coefficient and autospectrum plot) represent the natural continuation of this work. Further analyses will also clarify the dependence of the investigated parameters from the contrast in physical and mechanical properties between the heterogeneity and the background.

REFERENCES

Bergamo, P., D. Boiero, and L. V. Socco, 2012, Retrieving 2D structures from surface wave data by means of space-varying spatial windowing: Geophysics, **77**, no.4, EN39–EN51. https://doi.org/10.1190/geo2012-0031.1.

Bergamo, P., and L. V. Socco, 2014, Detection of sharp later discontinuities through the analysis of surface-wave propagation: Geophysics, **79**, no. 4, EN77-EN90. https://doi.org/10.1190/geo2012-0031.1.

Bièvre, G., D. Jongmans, T. Winiarski and V. Zumbo, 2012, Application of geophysical measurements for assessing the role of fissures in water infiltration within a clay landslide (Trieves area, French Alps): Hydrological Processes, **26**, 2128-2142.

Bohlen, T., S. Kugler, G. Klein, and F. Theilen, 2004, 1.5 D inversion of lateral variation of Scholte-wave dispersion: Geophysics, **69**, 330–344.

Boiero, D., and L. V. Socco, 2011, The meaning of surface wave dispersion curves in weakly laterally varying structures: Near Surface Geophysics, **9**, 561–570. https://doi.org/10.3997/1873-0604.2011042.

Carpentier, S. T. A., A. G. Green, R. Langridge, F. Hurter, A. Kaiser, H. Horstmeyer, and M. Finnemore, 2012, Seismic imaging of the Alpine Fault near Inchbonnie, New Zealand: Journal of Geophysical Research: Solid Earth, **118**, 416–431, https://doi.org/10.1029/2012JB009344.

Colombero, C., C. Comina, G. Umili, and S. Vinciguerra, 2016, Multiscale geophysical characterization of an unstable rock mass: Tectonophysics, **675**, 275–289. https://doi.org/10.1016/j.tecto.2016.02.045.

Colombero, C., L. Baillet, C. Comina, D. Jongmans, and S. Vinciguerra, 2017, Characterization of the 3-D fracture setting of an unstable rock mass: from surface and seismic investigations to numerical modeling: JGR Solid Earth, **122**, 1-21. https://doi.org/10.1002/2017jb014111.

Foti, S., 2004, Using transfer function for estimating dissipative properties of soils from surface-wave data: Near Surface Geophysics, **2**, 231–240. https://doi.org/10.3997/1873-0604.2004020.

Gischig, V. S., E. Eberhardt, J. R. Moore, and O. Hungr, 2015, On the seismic response of deep-seated rock slope instabilities - Insights from numerical modeling: Engineering Geology, **193**, 1–18. https://doi.org/10.1016/j.enggeo.2015.04.003.

Herman, G. C., P. A. Milligan, R. J. Huggins, and J. W. Rector, 2000, Imaging shallow objects and heterogeneities with scattered guided waves: Geophysics, **65**, 247–252. https://doi.org/10.1190/1.1444715.

Hévin, G., O. Abraham, H. A. Pedersen, and M. Campillo, 1998, Characterisation of surface cracks with Rayleigh waves: a numerical model: NDT&E International, **31**, 289-297.

Hyslop, C., and R. R. Stewart, 2015, Imaging lateral heterogeneity using reflected surface waves: Geophysics, **80**, no. 3, EN69–EN82. https://doi.org/10.1190/geo2014-0066.1.

Ikeda, T., and T. Tsuji, 2016, Surface wave attenuation in the shallow subsurface from multichannel–multishot seismic data: a new approach for detecting fractures and lithological discontinuities: Earth, Planets and Space, **68**, no. 111, 1–14. https://doi.org/10.1186/s40623-016-0487-0.

Kaslilar, A., 2007, Inverse scattering of surface waves: imaging of near-surface heterogeneities: Geophysical Journal International, **171**, 352–367. https://doi.org/10.1111/j.1365-246X.2007.03524.x.

Leparoux D., A. Bitri and G. Grandjean, 2000, Underground cavity detection: a new method based on seismic Rayleigh Waves: EJEEG, **5**, 33–53.

Liu Z., A. AlTheyab, S.M. Hanafy and G. Schuster, 2017, Imaging near-surface heterogeneities by natural migration of backscattered surface waves: Field data test: Geophysics, **82**, no. 3, S197-S205. https://doi.org/10.1190/GEO2016-0253.1.

Mullen, R., and T. Belytschko, 1982, Dispersion analysis of finite element semidiscretizations of the two-dimensional wave equation: Int. J. Numer. Methods Eng., **18**, 11–29.

Nasseri-Moghaddam, A., G. Cascante and J. Hutchinson, 2005, A new quantitative procedure to determine the location and embedment depth of a void using surface waves: Journal of Environmental and Engineering Geophysics, **10**, 51-64. https://doi.org/10.2113/JEEG10.1.51.

Park, C. B., J. Xia, and R. D. Miller, 1998, Ground roll as a tool to image near-surface anomaly: 68th Annual International Meeting, SEG, Expanded Abstracts, 874–877.

Schwenk, J. T., S. D. Sloan, J. Ivanov, and R. D. Miller, 2016, Surface-wave methods for anomaly detection: Geophysics, **81**, no. 4, EN29–EN42. https://doi.org/10.1190/geo2015-0356.1.

Strobbia, C., and S. Foti, 2006, Multi-offset phase analysis of surface wave data (MOPA): Journal of Applied Geophysics, **59**, 300–313, https://doi.org/10.1016/j.jappgeo.2005.10.009.

Vignoli, G., and G. Cassiani, 2010, Identification of lateral discontinuities via multi-offset phase analysis of surface wave data: Geophysical Prospecting, **58**, 389–413, https://doi.org/10.1111/j.1365-2478.2009.00838.x.

Vignoli, G., C. Strobbia, G. Cassiani, and P. Vermeer, 2011, Statistical multioffset phase analysis for surface-wave processing in laterally varying media: Geophysics, **76**, no. 2, U1–U11, https://doi.org/10.1190/1.3542076.

Xia J., R. D. Miller, C. B. Park, and G. Tian, 2002, Determining Q of near-surface materials from Rayleigh waves: J. Appl. Geophys., 51, no. 2, 121–129. https://doi.org/10.1016/S0926-9851(02)00228-8.

Xia, J., J. E. Nyquist, Y. X. Xu, M. J. S. Roth, and R. D. Miller, 2007, Feasibility of detecting near-surface feature with Rayleigh wave diffraction: J. Appl. Geophys., 62, no. 3, 244–253. https://doi.org/10.1016/j.jappgeo.2006.12.002.

Zerwer, A., M. A. Polak and J. C. Santamarina, 2005, Detection of surface breaking cracks in concrete members using Rayleigh waves: Journal of Environmental and Engineering Geophysics, **10**, 295-306. https://doi.org/10.2113/JEEG10.3.295.

Appendix A: Processing workflow

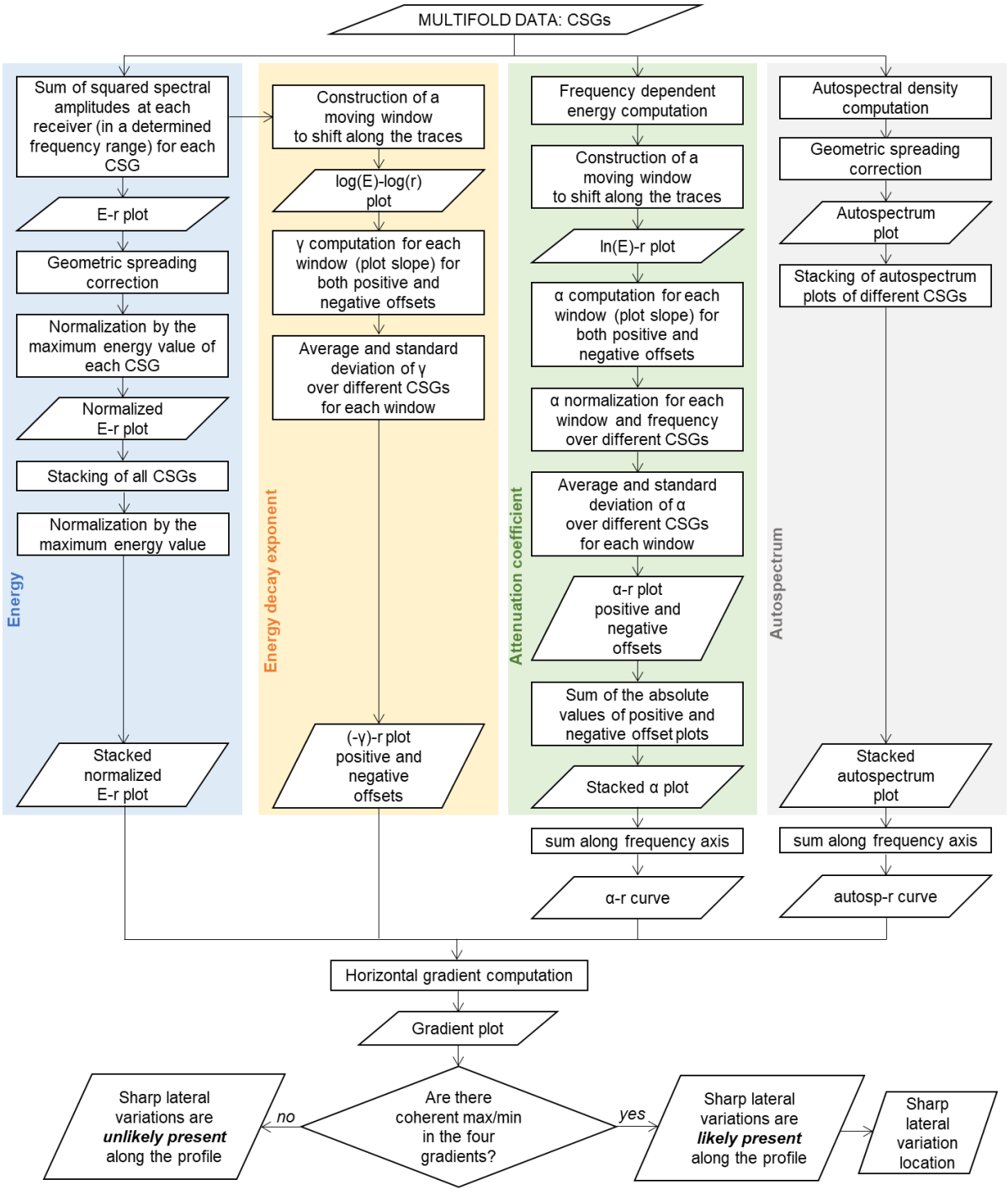

Figure A1. Complete processing workflow including computation for energy, energy decay exponent, attenuation coefficient and autospectrum for detection and location of sharp lateral variations.

APPENDIX B: Effect of SNR on the synthetic results

In this appendix, the effect of noise on the results obtained with the four methods is analyzed on the synthetic CSGs of model B_2 (geometry and model parameters in Figure 1b and Table 2).

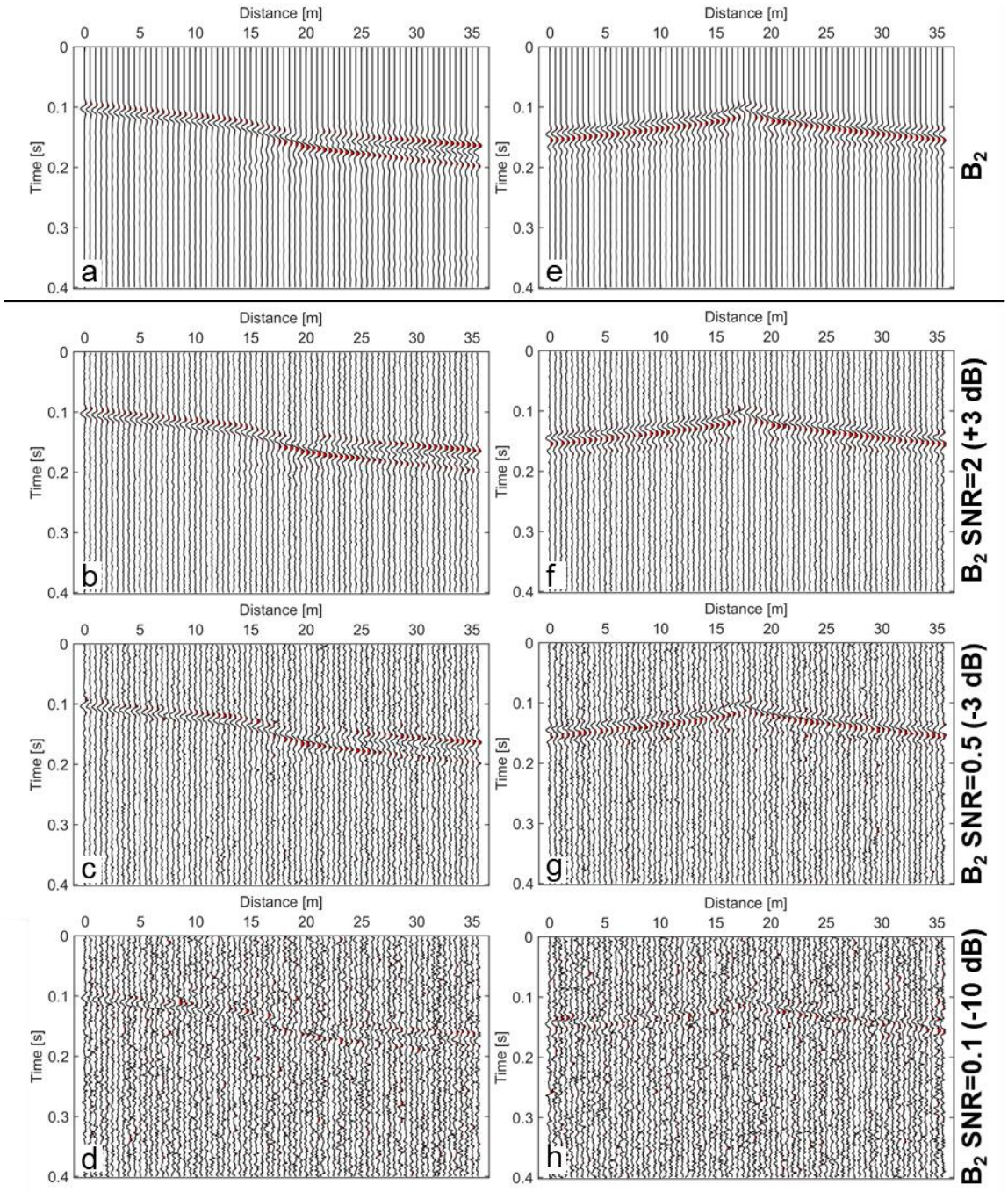

Figure B1. Synthetic CSGs for model B_2. (a-d) S1 and (e-h) S4. (a, e) Unperturbed traces. (b, f) SNR=2; (c, g) SNR=0.5; (d, h) SNR=0.1.

Exemplificative unperturbed CSGs for the model are shown in Figure B1a (S1, Figure 1b) and Figure B1e (S4, Figure 1b). We considered Signal-to-Noise ratio (SNR) as the ratio between the mean power of the signal and the mean power of noise. For all the CSGs, each trace was perturbed with additive Gaussian noise, considering SNRs equal to 2 (+3 dB, e.g. b and f in Figure B1), 0.5 (-3 dB, e.g. c and g in Figure B1) and 0.1 (-10 dB, e.g. d and h in Figure B1). Energy, energy decay exponent, attenuation coefficient and autospectrum results are shown in Figure B2, while gradient computations are summarized in Figure B3.

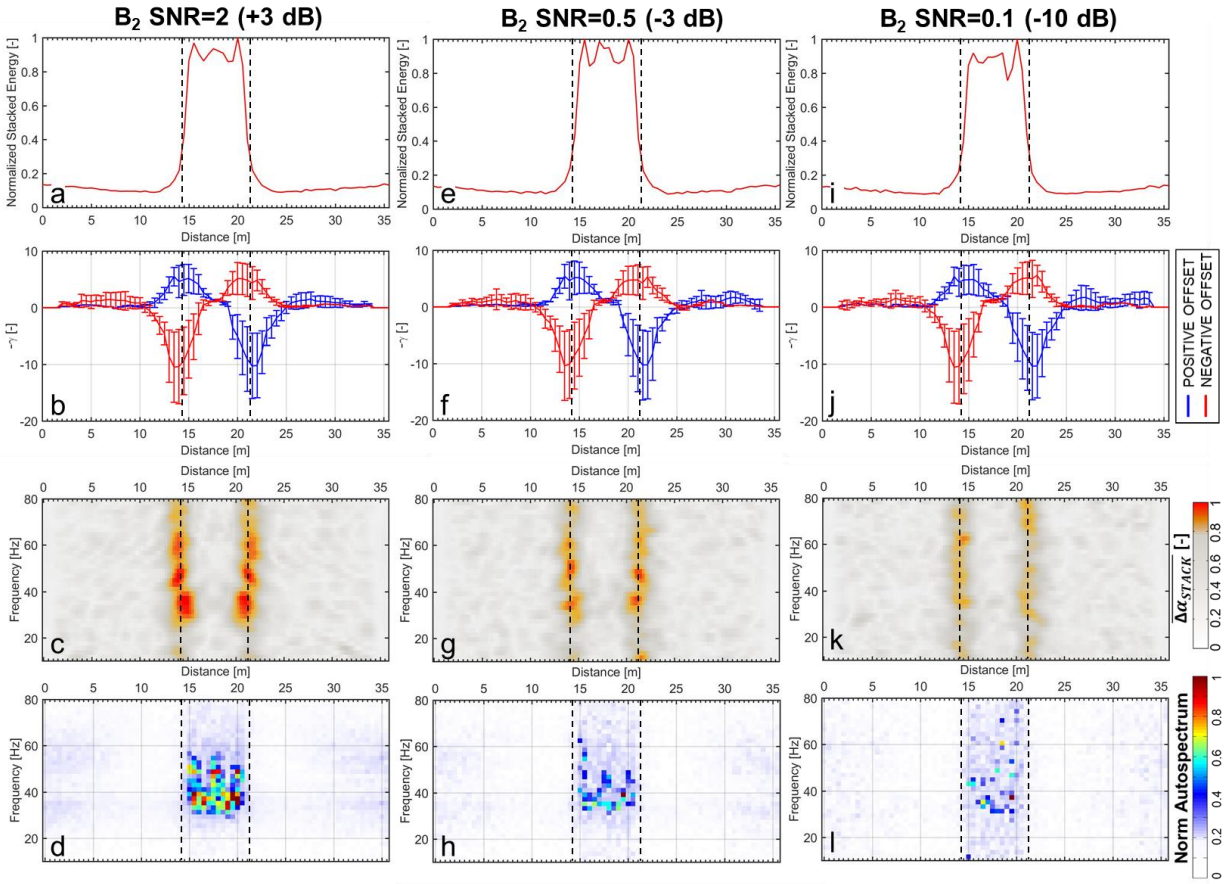

Figure B2. Results on the perturbed model B2 (a-d) SNR=2; (e-h) SNR=0.5; (i-l) SNR=0.1. (a, e, i) Multifold stacked energy plots. (b, f, j) Energy decay exponent results. (c, g, k) Stacked attenuation coefficient plots. (d, h, l) Multifold stacked autospectrum plots.

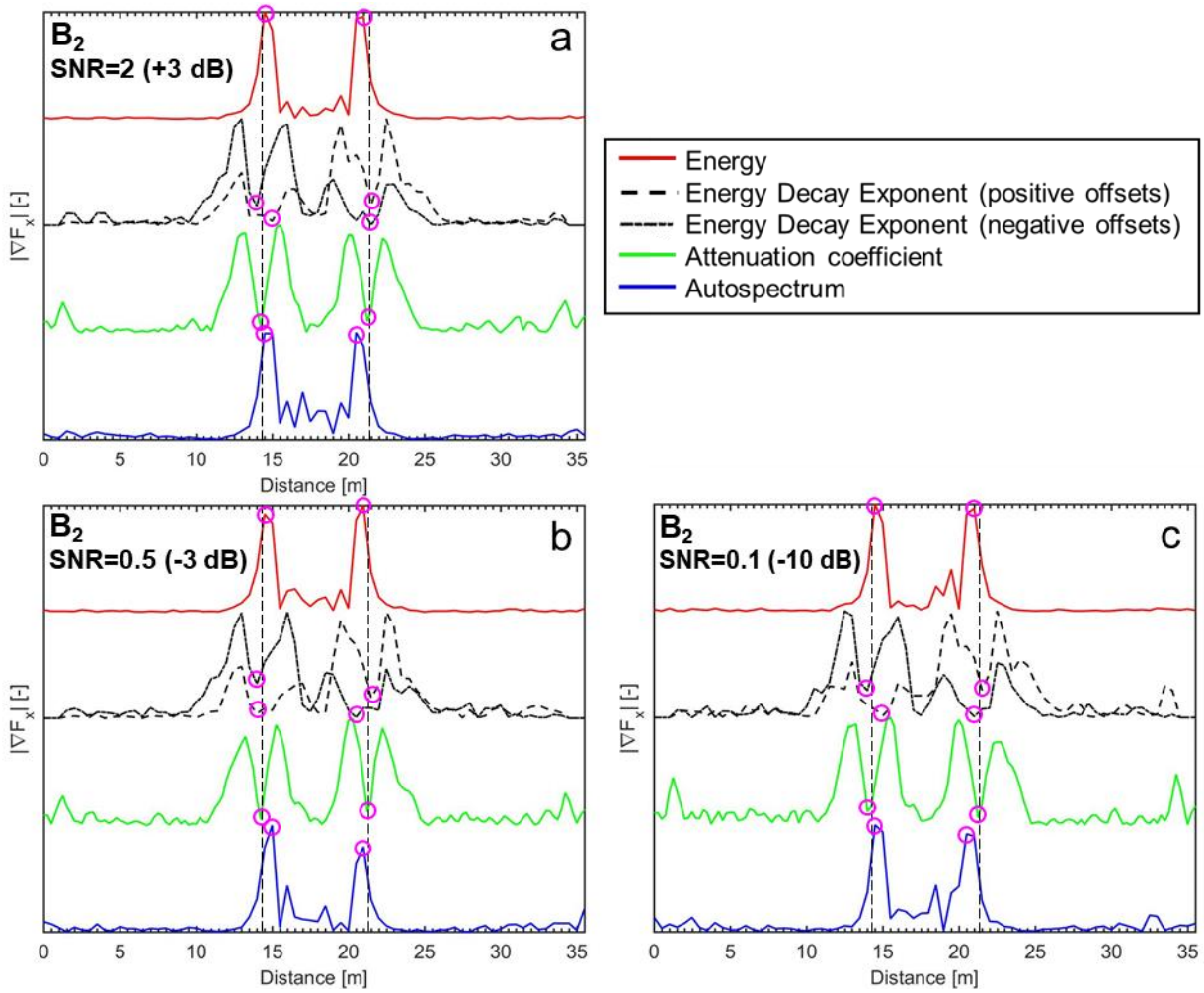

Figure B3. Normalized absolute value of the horizontal gradients of the four parameters on the perturbed model B_2 (a) SNR=2; (b) SNR=0.5; (c) SNR=0.1: energy (in red), energy decay exponent (in black; dashed line: positive offsets; dash-dotted line: negative offsets), attenuation coefficient (in green), autospectrum (in blue). In each section, the vertical dashed lines mark the real position of the lateral variations, while the magenta circles highlight the locations of the lateral variations, according to the adopted criteria.

Table B1. Location errors for unperturbed and perturbed CSGs of model B_2 (with SNR of 2, 0.5 and 0.1). LE: left edge and RE: right edge of the box.

Model	E		γ		α		Autospectrum	
	LE [m]	RE [m]	LE [m]	RE [m]	LE [m]	RE [m]	LE [m]	RE [m]
B_2	**-0.25**	**0.25**	**-0.25**	**-0.25**	**-0.25**	**0.25**	**-0.75**	**0.75**
B_2 SNR=2	-0.25	0.25	-0.25	-0.25	0.00	0.00	-0.25	0.75
B_2 SNR=0.5	-0.25	0.25	0.25	0.25	0.00	0.00	-0.75	0.25
B_2 SNR=0.1	-0.25	0.25	-0.25	0.00	0.25	0.00	-0.25	0.75

The target is detected in all the test configurations, even with very low SNRs. Location errors (Table B1) are stable in the range of the unperturbed model and independent from SNR decrease. Similar results can be obtained for all the other synthetic models, with location errors diverging from the unperturbed values (Table 3) of less than the receiver spacing (0.5 m).

List of captions

Figure 1. Geometries adopted for the synthetic models, reproducing different shapes of the heterogeneities and embedment conditions. Model parameters are summarized in Table 1 (model name and subscript refer to geometry and material parameters respectively). (a) A_1; (b) B_1, B_2 and $B2_R$; (c) $B1_2$ and $B1_{2R}$; (d) $B2_2$ and $B2_{2R}$; (e) C_3 and C_{3R}; (f) D_3 and D_{3R}. G1 to G72: geophone locations; S1 to S7: shot locations.

Figure 2. Energy results on (a, c) A_1 and (b, d) B_1. Left column: single-fold results; right column: multifold stacked results. In each section, the vertical dashed lines highlight the real position of the lateral variations.

Figure 3. Multifold stacked energy results. (a) B_2; (b) $B1_2$; (c) $B2_2$; (d) B_{2R}; (e) $B1_{2R}$; (f) $B2_{2R}$. In each section, the vertical dashed lines highlight the real position of the lateral variations.

Figure 4. Multifold stacked energy results. (a) C_3; (b) D_3; (c) C_{3R}; (d) D_{3R}. In each section, the vertical dashed lines highlight the real position of the lateral variations.

Figure 5. Energy decay exponent results on (a) A_1; (b) B_1. In each section, the vertical dashed lines highlight the real position of the lateral variations.

Figure 6. Energy decay exponent results on (a) B_2; (b) $B1_2$; (c) $B2_2$; (d) B_{2R}; (e) $B1_{2R}$; (f) $B2_{2R}$. In each section, the vertical dashed lines highlight the real position of the lateral variations.

Figure 7. Energy decay exponent results on (a) C_3; (b) D_3; (c) C_{3R}; (d) D_{3R}. In each section, the vertical dashed lines highlight the real position of the lateral variations.

Figure 8. Attenuation coefficient results on (a, b, e) A_1 and (c, d, f) B_1. Left column: separate plots for positive (top) and negative (bottom) offsets. Right column: stacked plot of the single-offset plots (absolute value) on the left. In each section, the vertical dashed lines highlight the real position of the lateral variations.

Figure 9. Stacked attenuation coefficient results on (a) B_2; (b) $B1_2$; (c) $B2_2$; (d) B_{2R}; (e) $B1_{2R}$; (f) $B2_{2R}$. In each section, the vertical dashed lines highlight the real position of the lateral variations.

Figure 10. Stacked attenuation coefficient results on (a) C_3; (b) D_3; (c) C_{3R}; (d) D_{3R}. In each section, the vertical dashed lines highlight the real position of the lateral variations.

Figure 11. Autospectrum results on (a, c) A_1; (b, d) B_1. Left column: single-fold autospectrum of shot S1. Right column: multifold stacked autospectrum. In each section, the vertical dashed lines highlight the real position of the lateral variations.

Figure 12. Multifold stacked autospectrum results on (a) B_2; (b) $B1_2$; (c) $B2_2$; (d) B_{2R}; (e) $B1_{2R}$; (f) $B2_{2R}$. In each section, the vertical dashed lines highlight the real position of the lateral variations.

Figure 13. Multifold stacked autospectrum results on (a) C_3; (b) D_3; (c) C_{3R}; (d) D_{3R}. In each section, the vertical dashed lines highlight the real position of the lateral variations.

Figure 14. CNR test site. (a) Geographic location. (b) Aerial view of the site with location of the sand box (yellow square) and the seismic array (red line). (c) Geometry of the target and seismic layout. G1 to G72: geophone locations; S1 to S11: shot locations. (d) Common shot gather for S1.

Figure 15. CNR results. (a) Multifold stacked energy-distance plot. (b) Energy decay exponent results. (c) Stacked attenuation coefficient results. (d) Multifold stacked autospectrum plot. In each section, the vertical dashed lines highlight the approximate real position of the box edges.

Figure 16. Madonna del Sasso test site. (a) Geographic location. (b, c) Aerial views of the site with location of the main fractures (F1 to F4, dashed lines) and seismic array (red continuous line). (d) Geometry of the seismic layout and fracture locations. G1 to G48: geophone locations; S1 to S13: shot locations. (e) Common shot gather for S1.

Figure 17. Madonna del Sasso results. (a) Multifold stacked energy-distance plot. (b) Energy decay exponent results. (c) Stacked attenuation coefficient results. (d) Multifold stacked autospectrum plot. In each section, the vertical dashed lines highlight the approximate real position of fractures.

Figure 18. Normalized absolute value of the horizontal gradients of the four parameters on (a) A_1 and (b) B_1 synthetic models: energy (in red), energy decay exponent (in black; dashed line: positive offsets; dash-dotted line: negative offsets), attenuation coefficient (in green), autospectrum (in blue). In each section, the vertical dashed lines mark the real position of the lateral variations, while the magenta circles highlight the locations of the lateral variations, according to the criteria described in the text.

Figure 19. Normalized absolute value of the horizontal gradients of the four parameters on (a) B_2, (b) $B1_2$, (c) $B2_2$, (d) B_{2R}, (e) $B1_{2R}$, (f) $B2_{2R}$ synthetic models: energy (in red), energy decay exponent (in black; dashed line: positive offsets; dash-dotted line: negative offsets), attenuation coefficient (in green), autospectrum (in blue). In each section, the vertical dashed lines mark the real position of the lateral variations, while the magenta circles highlight the locations of the lateral variations, according to the criteria described in the text.

Figure 20. Normalized absolute value of the horizontal gradients of the four parameters on (a) C_3; (b) D_3; (c) C_{3R}; (d) D_{3R}: energy (in red), energy decay exponent (in black; dashed line: positive offsets; dash-dotted line: negative offsets), attenuation coefficient (in green), autospectrum (in blue). In each section, the vertical dashed lines mark the real position of the lateral variations, while the magenta circles highlight the locations of the lateral variations, according to the criteria described in the text.

Figure 21. Normalized absolute value of the horizontal gradients of the four parameters on (a) CNR test site; (b) Madonna del Sasso cliff: energy (in red), energy decay exponent (in black; dashed line: positive offsets; dash-dotted line: negative offsets), attenuation coefficient (in green), autospectrum (in blue). In each section, the vertical dashed lines mark the real position of the lateral variations, while the magenta circles highlight the locations of the lateral variations, according to the criteria described in the text.

Figure 22. Comparison of single-fold/offset and stacked results for the synthetic model (a-c) A_1 and (d-f) B_1. (a, d) S1 and multifold stacked normalized energy gradients. (b, e) S1 and multifold stacked normalized autospectrum gradients. (c, f) Attenuation coefficient normalized gradients for positive offset, negative offset and stacked results.

Figure 23. Comparison of single-fold/offset and stacked results for the field data (a-c) CNR and (d-f) Madonna del Sasso. (a, d) S1 and multifold stacked normalized energy gradients. (b, e) S1 and multifold stacked normalized autospectrum gradients. (c, f) Attenuation coefficient normalized gradients for positive offset (PO), negative offset (NO) and stacked results. In (d) and (e) the y-axis is in logarithmic scale to intensify the small fluctuations of single-fold gradients.

Figure A1. Complete processing workflow including computation for energy, energy decay exponent, attenuation coefficient and autospectrum for detection and location of sharp lateral variations.

Figure B1. Synthetic CSGs for model B_2. (a-d) S1 and (e-h) S4. (a, e) Unperturbed traces. (b, f) SNR=2; (c, g) SNR=0.5; (d, h) SNR=0.1.

Figure B2. Results on the perturbed model B_2 (a-d) SNR=2; (e-h) SNR=0.5; (i-l) SNR=0.1. (a, e, i) Multifold stacked energy plots. (b, f, j) Energy decay exponent results. (c, g, k) Stacked attenuation coefficient plots. (d, h, l) Multifold stacked autospectrum plots.

Figure B3. Normalized absolute value of the horizontal gradients of the four parameters on the perturbed model B_2 (a) SNR=2; (b) SNR=0.5; (c) SNR=0.1: energy (in red), energy decay exponent (in black; dashed line: positive offsets; dash-dotted line: negative offsets), attenuation coefficient (in green), autospectrum (in blue). In each section, the vertical dashed lines mark the real position of the lateral variations, while the magenta circles highlight the locations of the lateral variations, according to the adopted criteria.

Supplementary material

Figure S1. Single-fold normalized energy-distance plots related to shots S1 to S7. (a) B_2; (b) $B1_2$; (c) $B2_2$; (d) B_{2R}; (e) $B1_{2R}$; (f) $B2_{2R}$. In each section, the vertical dashed lines highlight the real position of the lateral variations.

Figure S2. Single-fold normalized energy-distance plots related to shots S1 to S7. (a) C_3, (b) D_3, (c) C_{3R}, (d) D_{3R}. In each section, the vertical dashed lines highlight the real position of the lateral variations.

Figure S3. Positive (top) and negative (bottom) offset attenuation coefficient results. (a, b) B_2; (c, d) $B1_2$; (e, f) $B2_2$; (g, h) B_{2R}; (i, j) $B1_{2R}$; (k, l) $B2_{2R}$. In each section, the vertical dashed lines highlight the real position of the lateral variations.

Figure S4. Positive (top) and negative (bottom) offset attenuation coefficient results. (a, b) C_3, (c, d) D_3, (e, f) C_{3R}, (g, h) D_{3R}. In each section, the vertical dashed lines highlight the real position of the lateral variations.

Figure S5. Single-fold (S1) autospectrum plots. (a) B_2; (b) $B1_2$; (c) $B2_2$; (d) B_{2R}; (e) $B1_{2R}$; (f) $B2_{2R}$. In each section, the vertical dashed lines highlight the real position of the lateral variations.

Figure S6. Single-fold (S1) autospectrum plots. (a) C_3, (b) D_3, (c) C_{3R}, (d) D_{3R}. In each section, the vertical dashed lines highlight the real position of the lateral variations.

Figure S7. CNR test site. (a) Exemplificative single-fold normalized energy-distance plots (for S1, S2, 10 and S11 in Figure 14). (b) Positive and (c) negative offset attenuation coefficient results. (d) Exemplificative single-fold (S1) autospectrum plot.

Figure S8. Madonna del Sasso test site. (a) Exemplificative single-fold normalized energy-distance plots (for S1 and S13 in Figure 16). (b) Positive and (c) negative offset attenuation coefficient results. (d) Exemplificative single-fold (S1) autospectrum plot.